



Published in final edited form as:

Neuron. 2023 August 02; 111(15): 2383–2398.e7. doi:10.1016/j.neuron.2023.05.006.

An astrocyte BMAL1-BAG3 axis protects against alpha-synuclein and tau pathology

Patrick W. Sheehan^{1,†}, Collin J. Nadarajah^{1,†}, Michael F. Kanan¹, Jessica N. Patterson¹, Brenna Novotny², Jennifer H. Lawrence¹, Melvin W. King¹, Logan Brase², Casey E. Inman¹, Carla M. Yuede², Jiyeon Lee¹, Tirth K. Patel¹, Oscar Harari^{2,5}, Bruno A. Benitez^{3,4}, Albert A. Davis, MD, PhD^{1,*}, Erik S. Musiek, MD, PhD^{1,5,6,7,*}

¹Department of Neurology, Washington University School of Medicine, St. Louis, MO, USA.

²Department of Psychiatry, Washington University School of Medicine, St. Louis, MO, USA.

³Department of Neurology, Beth Israel Deaconess Medical Center, Boston, MA, USA.

⁴Harvard Medical School, Boston, MA, USA

⁵Knight Alzheimer's Disease Research Center, Washington University School of Medicine, St. Louis, MO, USA.

⁶Center On Biological Rhythms And Sleep (COBRAS), Washington University School of Medicine, St. Louis, MO, USA.

⁷Lead contact.

SUMMARY

The circadian clock protein BMAL1 modulates glial activation and amyloid-beta deposition in mice. However, the effects of BMAL1 on other aspects of neurodegenerative pathology are unknown. Here, we show that global post-natal deletion of *Bmal1* in mouse tauopathy or alpha-synucleinopathy models unexpectedly suppresses both tau and alpha-synuclein aggregation and related pathology. Astrocyte-specific *Bmal1* deletion is sufficient to prevent both alpha-synuclein and tau pathology in vivo, and induces astrocyte activation and expression of *Bag3*, a chaperone critical for macroautophagy. Astrocyte *Bmal1* deletion enhances phagocytosis of alpha-synuclein and tau in a *Bag3*-dependent manner, and astrocyte *Bag3* overexpression is sufficient to mitigate alpha-synuclein spreading in vivo. In humans, *BAG3* is increased in patients with AD, and is

[†]Erik Musiek and Albert Davis are co-corresponding authors. *Address correspondence to: Erik Musiek, MD, PhD; musieke@wustl.edu or Albert "Gus" Davis, MD, PhD, albert.a.davis@wustl.edu.

[†]These authors contributed equally.

Author Contributions

Conceptualization: P.W.S., A.A.D., and E.S.M.; Methodology: P.W.S., C.J.N., M.F.K., O.H., B.A.B., A.A.D., and E.S.M.; Investigation: P.W.S., C.J.N., M.F.K., J.N.P., B.N., J.H.L., M.W.K., L.B., C.M.Y., J.Y., T.K.P., B.A.B.; Data Curation: P.W.S., O.H., B.A.B.; Project Administration: P.W.S. and E.S.M.; Funding: A.A.D., E.S.M.; Writing-Initial: P.W.S., C.J.N., A.A.D., E.S.M. Review and Editing: P.W.S., C.J.N., O.H., B.A.B., A.A.D., E.S.M.

Declarations of Interest

The authors report no relevant conflicts of interest.

Publisher's Disclaimer: This is a PDF file of an unedited manuscript that has been accepted for publication. As a service to our customers we are providing this early version of the manuscript. The manuscript will undergo copyediting, typesetting, and review of the resulting proof before it is published in its final form. Please note that during the production process errors may be discovered which could affect the content, and all legal disclaimers that apply to the journal pertain.

highly expressed in disease-associated astrocytes. Our results suggest that early activation of astrocytes via *Bmal1* deletion induces *Bag3* to protect against tau and alpha-synuclein pathologies, providing new insights into astrocyte-specific therapies for neurodegeneration.

eTOC Blurp

Sheehan, Nadarajah, et al. show that deletion of the circadian clock gene *Bmal1* in astrocytes protects against tau and alpha-synuclein pathology by triggering a unique astrocyte activation profile marked by increased BAG3 expression. Astrocyte BAG3 expression was itself protective and upregulated in disease-associated astrocytes in human Alzheimer's Disease.

Keywords

BMAL1; astrocytes; circadian; Alzheimer Disease; tau; Parkinson Disease; alpha-synuclein; neuroinflammation; BAG3

INTRODUCTION

Astrocytes, the most abundant glial cells in the brain, have long been implicated in the pathogenesis of age-related neurodegenerative conditions such as Alzheimer's Disease (AD)^{1,2}. Reactive astrocytes are ubiquitous hallmarks of neurodegenerative diseases, though the exact roles of reactive astrocytes in regulating toxic protein aggregation, neuroinflammation, and neurodegeneration are highly complex². Previous work from our group has identified the core circadian transcription factor BMAL1 (aka ARNTL) as a potent regulator of astrocyte activation^{3,4}. Global deletion of *Bmal1* renders mice behaviorally and transcriptionally arrhythmic⁵ and also alters the expression of many non-rhythmic genes, driving distinct transcriptional changes in different brain cell types⁶. Among the most striking phenotypes observed following *Bmal1* deletion in mice is astrocyte activation, which is characterized by increased expression of glial fibrillary acidic protein (GFAP), is cell-autonomous, and is associated with a unique transcriptional profile^{3,4,7}. Functionally, global post-natal deletion of *Bmal1* in the APP/PS1–21 mouse model of AD exacerbates extracellular β -amyloid plaque formation⁸, while astrocyte-specific *Bmal1* deletion had no impact on plaque accumulation in this model⁷. However, the cell type-specific effects of *Bmal1* disruption on other aspects of neurodegenerative neuropathology remain unexplored.

Although β -amyloid accumulates in plaques in the extracellular space⁹, other neurodegenerative disease-associated proteins, including tau and alpha-synuclein (α Syn), aggregate within neurons and exhibit spreading to neighboring cells, including trans-synaptic propagation to other neurons¹⁰. Previous studies have suggested that glia can interact with protein aggregates in the extracellular space¹¹. Tau aggregation is a hallmark of AD and several other neurodegenerative diseases termed "tauopathies". α Syn pathology defines Parkinson Disease (PD) and related "synucleinopathies" including Dementia with Lewy Bodies and Multiple Systems Atrophy, and is also present in nearly half of AD cases¹². Notably, a recent study identified BMAL1 as one of the top upstream transcription factors driving astrocyte responses to tauopathy and amyloid plaques in mice, suggesting

that, in addition to its role in the circadian clock, BMAL1 could modulate astrocyte responses to neurodegenerative pathology¹³. However, it is unknown if manipulation of BMAL1 can influence tau or α Syn pathology.

Here, we explored the effects of *Bmal1* deletion on pathology caused by tau and α Syn, both of which exhibit intracellular aggregation. Unexpectedly, we discovered that global *Bmal1* deletion was protective against both tau and α -synuclein aggregation and consequent microglial activation. We find that this protective effect is driven by BMAL1-mediated astrocyte activation and expression of BAG3, a macroautophagy chaperone. Astrocyte BAG3 overexpression was itself protective against pathology, and *BAG3* was highly expressed specifically in a subset of disease-associated activated astrocytes from human AD brain samples. Our findings demonstrate that early astrocyte activation can mitigate tau and α Syn pathology *in vivo* and show that loss of BMAL1 induces a protective astrocyte activation state.

RESULTS

Global *Bmal1* deletion prevents tau aggregation in P301S mice.

We employed a tamoxifen-inducible global *Bmal1* KO mouse which exhibits circadian arrhythmicity but avoids developmental confounds related to germline *Bmal1* deletion^{8,14}. We crossed this mouse to the widely used P301S PS19 model of tauopathy¹⁵ to generate four mouse genotypes: CAG-Cre^{ERT2} -; *Bmal1*^{f/f}; P301S- (termed CTRL), CAG-Cre^{ERT2} +; *Bmal1*^{f/f}; P301S- (termed gKO for global *Bmal1* KO), CAG-Cre^{ERT2} -; *Bmal1*^{f/f}; P301S+ (termed P301S), and CAG-Cre^{ERT2} +; *Bmal1*^{f/f}; P301S+ (termed gKO;P301S). We administered tamoxifen to delete *Bmal1* at two months of age (3–5 months before the onset of tau pathology), then harvested mice for pathology at eight months of age, when P301S+ mice typically exhibit moderate tau pathology (Fig. 1a). We used only male P301S mice because they develop pathology earlier and more consistently than females. As we have demonstrated previously^{4,14}, post-natal deletion of *Bmal1* triggered significant astrogliosis, assessed using GFAP immunohistochemistry (IHC) (Fig. 1b). We also confirmed suppression of several known *Bmal1* transcriptional targets in cortex from gKO and gKO;P301S mice (Supplemental Fig. 1a). Phosphorylated tau (p-ser202, p-thr205) pathology assessed by AT8 immunohistochemistry showed a large increase in P301S mice compared to CTRL (Supplemental Figure 1b), but no significant difference between P301S and gKO;P301S mice in either the hippocampus (Supplemental Figure 1b) or piriform cortex (Fig. 1c), two regions that readily accumulate tau pathology in this model¹⁵. We next examined levels of soluble and insoluble tau by ELISA in cortical tissue subjected to sequential detergent extraction. Similar to the AT8 immunostaining, tau levels were not significantly different between P301S and gKO;P301S mice in the more soluble RAB and RIPA fractions. However, there was significantly less insoluble tau (70% formic acid fraction) in gKO;P301S mice compared to P301S, suggesting that highly insoluble tau species were *decreased* by deletion of *Bmal1* (Fig. 1d). Accordingly, misfolded, paired helical filament tau was quantified by IHC using the antibody MC1¹⁶ and was also markedly reduced in gKO;P301S mice (Fig. 1e). We also observed a decrease in Thioflavin S+ tau aggregates in the gKO;P301S brain compared to P301S mice, suggesting a reduction

in insoluble β -pleated sheet-containing aggregates (Fig. 1f). We further classified AT8 immunohistochemistry as fitting into one of four patterns of increasing severity in the hippocampus¹⁷. Again, gKO;P301S mice had substantially less of the severe “type 4” staining than P301S mice (Supplemental Figure 1c). These data demonstrate that global deletion of *Bmal1* reduced aggregated, insoluble tau pathology without altering total tau or soluble tau levels.

Global *Bmal1* deletion mitigates microglial activation in P301S mice

Aggregated tau pathology is associated with pronounced microglia and astrocyte activation in P301S mice¹⁷. Thus, we examined a panel of transcripts associated with neuroinflammation and microglial activation in cortex tissue from CTRL, gKO, P301S, and gKO;P301S mice. P301S mice exhibited marked upregulation of all neuroinflammatory markers tested, including disease-associated microglia (DAM) markers *Spp1*, *Trem2*, *Tyrobp*, *Clec7a*, and *ApoE*¹⁸. Expression of all neuroinflammatory markers was attenuated in gKO;P301S compared to P301S mice (Fig. 2a). PCA plots of inflammatory gene expression showed minimal overlap between P301S mice and each of the other genotypes (Supplemental Fig. 2a), further indicating decreased inflammation in gKO;P301S mice. We quantified microglial branching morphology in the hippocampus and found that microglia in P301S mice had fewer branches per cell than gKO;P301S mice, indicating an activated microglia phenotype (Fig. 2b). CD68, a marker of microglial phagocytic activation¹⁹, was increased in Iba1+ microglia in hippocampus of P301S mice but was largely absent in gKO;P301S mice, further demonstrating that *Bmal1* deletion attenuated or prevented microglial activation (Fig. 2c, Supplemental Fig. 2b).

Male P301S mice develop brain atrophy in parallel with tau pathology¹⁷. We observed no difference between P301S and gKO;P301S mice in thickness of the hippocampal CA1 and hippocampal granule layers, despite clear differences in aggregated tau and microgliosis (Supplemental Fig. 2c). This may suggest that the detrimental effects of neuronal *Bmal1* deletion on neuronal health³ may offset the potential protective effects of mitigating tau pathology.

Finally, we assessed astrocyte activation by immunostaining for GFAP and found that unlike microgliosis, GFAP expression was increased in gKO mice to a similar high degree as in P301S or gKO;P301S mice, as astrogliosis induced by *Bmal1* deletion alone reaches a ceiling effect and is not further exacerbated by tau pathology (Fig. 2D). Other astrocyte activation transcripts, *Aqp4* and *C4b*, also showed this pattern (Fig. 2E). These data show that *Bmal1* deletion drives astrogliosis early in the disease course in this model, and suggest that astrocyte activation may play a role in mitigating tau aggregation and subsequent microglial activation in gKO;P301S mice.

Global deletion of *Bmal1* suppresses α -synuclein spreading pathology and microgliosis

We next decided to test the effect of *Bmal1* deletion in an alpha-synuclein preformed fibril (α Syn PFF) model, in which α Syn PFFs are injected into the striatum, causing seeding and spreading of endogenous mouse α -synuclein pathology^{20,21}. As before, we used the same CTRL and gKO mice as before, and tamoxifen was administered at two

months of age, followed by a unilateral intrastriatal injection of α Syn PFFs one month later (Fig. 3a). As expected, gKO mice develop substantial astrogliosis one month post-tamoxifen, prior to PFF injection (Fig. 3b). We examined the burden of aggregated, phosphorylated (Ser129) α -synuclein (pSyn) in these mice three months after PFF injection and observed a reduction in pSyn pathology in the striatum and somatosensory cortex in gKO compared to control animals, similar to the reduction seen in the tau model (Fig. 3c). Astrogliosis was minimal in the ipsilateral cortex and striatum of CTRL mice injected with PFFs but was significantly increased as expected in gKO mice as a direct effect of *Bmal1* deletion (Fig. 3d). Microglial activation, as assessed by Iba1/CD68 co-staining in cortex (Fig. 3e) and by microglial branching analysis in striatum (Fig. 3f) was significantly decreased in the cortex of PFF-injected gKO mice as compared to PFF-injected CTRL mice.

Behavioral deficits in this model are minimal at the three-month time point but are generally related to pathology in the substantia nigra pars compacta (SNpc) (Luk et al., 2012). We performed a pole descending test in PBS- or α Syn PFF-injected CTRL and gKO mice 80 days post-PFF injection, and observed no effect of either PFF injection or genotype on this test (Supplemental Fig. 2d). Notably, we observed no difference in pSyn pathology in the SNpc between CTRL and gKO mice after PFF injection at this time point (Supplemental Fig. 2e), which is congruent with the lack of behavioral phenotype. Despite the lack of changes in SNpc pathology or motor behavior, our pathology data show that global *Bmal1* deletion mitigated α Syn pathology and attenuated microglial activation, similar to P301S mice.

Astrocyte-specific deletion of *Bmal1* prevents both α -synuclein and tau pathologies

We previously showed that *Bmal1* deletion drives cell-autonomous astrocyte activation⁴, suggesting that astrocyte activation might underlie the protective effects of global *Bmal1* deletion in tau and α Syn models. To test this, we used an inducible, astrocyte-specific *Aldh1l1*-Cre^{ERT2} mouse line²² to generate astrocyte-specific *Bmal1* KO mice (*Aldh1l1*-Cre^{ERT2} +; *Bmal1*^{fl/fl}; termed aKO), which we have previously characterized^{4,7}. *Bmal1* aKO mice showed striking astrocyte activation after tamoxifen treatment with sparing of neuronal BMAL1 expression (Fig. 4a). We crossed aKO mice to the P301S PS19 line, generating P301S (Cre-; *Bmal1*^{fl/fl}; P301S+) and aKO;P301S (*Aldh1l1*-Cre^{ERT2} +; *Bmal1*^{fl/fl}; P301S+) mice. Cre-; *Bmal1*^{fl/fl} littermate control mice were again termed CTRL. We treated mice with tamoxifen at two months of age and harvested this time at 9mo to analyze pathology (Fig. 4b). Similar to gKO mice, there was no difference between P301S and aKO;P301S mice in total phosphorylated tau as assessed with AT8 (Fig. 4c). However, MC1 immunostaining for aggregated tau demonstrated a significant decrease in tau pathology in the hippocampus and piriform cortex of aKO;P301S mice, suggesting that astrocytic *Bmal1* deletion is sufficient to reduce tau pathology (Fig. 4c). While AT8 and MC1 staining was detectable, it is notable that this cohort of mice developed substantially less aggregated tau pathology and neuroinflammation than the cohort in Fig. 1, perhaps due to genetic drift in the colony. To this point, we observed no significant differences in microglial activation/DAM transcripts in aKO mice at baseline, as well as no significant increase in P301S or aKO;P301S as compared to CTRL in this cohort, (Supplemental Fig. 3a,b). We observed no difference in total hippocampal NeuN area, consistent with a lack of gross neurodegeneration in

this cohort. However, the thickness of the neuronal (NeuN+) layer of either the dentate gyrus granule cells or CA1 was significantly increased in aKO;P301S mice as compared to P301S, suggesting a neuroprotective effect (Fig. 4d). Together, these results show that astrocyte-specific *Bmal1* deletion can reduce aggregated tau pathology in P301S, and can also prevent downstream neurodegeneration.

To determine whether astrocytic *Bmal1* deletion was also sufficient to mitigate α Syn pathology, we injected α -syn PFFs in CTRL and aKO mice using the same methods and timing as previously described (Fig. 5a). We focused on cortical regions (somatosensory and piriform) in these and subsequent experiments cortex as pathology in these areas requires spreading from the striatal injection region. Astrocytic *Bmal1* deletion recapitulated the phenotype observed in the global BMAL1 gKO mice, with aKO mice showing increased astrogliosis but reduced phospho-synuclein pathology across multiple brain regions, as compared to PFF-injected CTRL mice (Fig. 5a,b). As in the gKO cohort, no effect on pole descending behavior was noted (Supplemental Fig. 3c).

We next investigated whether the timing of astrocyte activation is critical for *Bmal1* deletion to mitigate protein aggregation. To do this, we switched the order of tamoxifen treatment and PFF injection, injecting α Syn PFFs one month before tamoxifen administration, such that astrogliosis occurred after initiation of α Syn seeding in CTRL or aKO mice (Fig. 5c). When the order of tamoxifen and PFF injection was reversed, astrogliosis still occurred in aKO mice, but there was no statistically significant reduction in pSyn pathology (Fig. 5c,d). These results show that deletion of *Bmal1* specifically in astrocytes is sufficient to reduce both tau and α Syn pathologies, and that astrocyte activation before pathology initiation is critical.

To evaluate a possible microglia-specific effect of *Bmal1* deletion on α Syn spreading, we generated inducible, microglia-specific, *Bmal1* knockout mice (Cx3cr1-Cre^{ERT2+};Bmal1^{fl/fl}). We confirmed that *Bmal1* expression was suppressed in microglia isolated from the brain of these mice after tamoxifen treatment, and observed no obvious spontaneous microglial activation in vivo in bulk cortex tissue (Supplemental Fig. 4a,b). We treated a cohort of microglial *Bmal1* KO mice (and Cre- littermate controls) with tamoxifen and injected α -syn PFFs as in Fig. 3. We observed no effect of microglial *Bmal1* deletion on aggregated α Syn pathology in this model, suggesting that reduction in α Syn pathology is not dependent on microglial *Bmal1* (Supplemental Fig. 4c).

***Bmal1*-dependent astrocytic *Bag3* expression modulates α -synuclein uptake**

To identify possible molecular mechanisms mediating the phenotypes described above, we next analyzed an existing RNAseq dataset derived from bulk cerebral cortex from aKO and Cre-controls⁷. We performed GO analysis of significant DEGs (using a permissive uncorrected $p < 0.05$ cutoff for exploratory analysis) to better understand pathways dysregulated in aKO mice. *Regulation of Protein Catabolic Process* (GO:0042176) emerged as one of the most upregulated pathways (Supplemental Fig. 5a), containing 71 genes which were differentially expressed in aKO cortex (Supplemental Fig. 5b). Among these, only 4 genes changed less than 1.5 fold and had an adjusted p-value of less than 0.1, two of which were upregulated in aKO mice, and two were downregulated (Supplemental Fig. 5c). Of

these, we focused on *Bag3*, as it is a known driver of macroautophagy^{23–26} and was recently identified as a PD-associated gene by a genome-wide association study²⁷. We confirmed that *Bag3* mRNA was also upregulated in cortex from brain-specific Nestin-*Bmal1* KO mice but was not increased in neuron-specific *Bmal1* KO mice (Supplemental Fig. 6a)⁴. We examined *Bag3* expression in samples from Fig. 1, and observed that *Bag3* was strongly upregulated in gKO mice and in P301S mice with no further increase in gKO;P301S mice (Fig. 6a), similar to other astrocyte activation transcripts (see Fig. 2e). Immunofluorescence for BAG3 and GFAP revealed that BAG3 protein was highly expressed in activated astrocytes in aKO mice (Fig. 6b), and that most of the BAG3 volume co-localized strongly with GFAP (Fig. 6c). We also observed markedly increased astrocytic BAG3 immunoreactivity in global *Bmal1* knockout (gKO) mice (Supplemental Fig. 6b,c).

To investigate mechanisms by which *Bmal1* deletion in astrocytes might mitigate tau and/or α -Syn pathology, we examined astrocyte phagocytosis of α -Syn aggregates *in vitro*. We conjugated α -Syn PFFs to the pH-sensitive dye pHrodo Red, the fluorescence of which is indicative of uptake into phagosomes or lysosomes²⁸. We then treated primary murine astrocyte-enriched cultures with siRNAs targeting *Bmal1* and/ *Bag3*, added pHrodo-PFFs to the culture medium, then quantified fluorescence via flow cytometry (Fig. 6d). SiRNA targeting *Bmal1* (siBmal1) reduced BMAL1 protein expression and resulted in increased BAG3 protein and *Bag3* mRNA expression compared to the scrambled siRNA (siSCR, Fig. 6e,f). *Bag3* siRNA strongly suppressed *Bag3* protein levels in primary astrocyte cultures, while treatment with both *Bmal1* and *Bag3* siRNA together resulted in a strong knockdown of both proteins and suppressed *Bag3* mRNA (Fig. 6e,f). Three days after siRNA knockdown, we added pHrodo-PFFs to the astrocytes for three hours to allow uptake, then washed the cells and incubated them for an additional 24 hours. Fluorescent signal from pHrodo-PFFs was visualized inside GFAP+ astrocytes in culture and co-localized with the lysosomal marker LAMP1 (Fig. 6g). Knockdown of *Bmal1* significantly increased astrocyte pHrodo-PFF signal, indicating increased phagocytosis and lysosomal uptake, while knockdown of *Bmal1* and *Bag3* together significantly attenuated the *Bmal1*-dependent increase in α -Syn PFF lysosomal uptake (Fig. 6h). Similar results were obtained when cells were harvested 8 hours after pHrodo washout (Supplemental Fig. 6d). *Bag3* knockdown alone did not affect α -Syn uptake (Supplemental Fig. 6e). These findings suggest that loss of *Bmal1* increases astrocytic α -Syn PFF uptake and degradation in a manner that is at least partially dependent on *Bag3*. To understand if *Bag3* upregulation alone is sufficient to increase pHrodo-PFF uptake, we created an AAV8 vector that drives *Bag3* expression under the *Gfap* promoter. This vector increased *Bag3* expression in a dose-dependent manner in primary astrocyte cultures, as compared to an AAV8-*Gfap*-eGFP control vector (Fig. 6i). Using the same pHrodo-PFF uptake system, we found that astrocytes overexpressing *Bag3* display increased uptake of pHrodo-PFFs (Fig. 6j). Our data suggest that *Bmal1* knockdown enhances astrocyte α -Syn PFF lysosomal uptake at least in part via a *Bag3*-dependent mechanism, and that astrocytic *Bag3* overexpression is sufficient to drive increased α -Syn lysosomal uptake *in vitro*.

Astrocyte BAG3 mediates α -Syn and tau clearance in vivo.

We next examined the role of BAG3 in mediating the effects of *Bmal1* deletion on the reduction of tau pathology in vivo. We utilized three AAV-PhP.eB viral vectors, which we injected into the striatum of *Bmal1^{fl/fl}* mice. These included 1. a control vector (AAV-GFAP-GFP), which expressed GFP under the compact GfaABC₁D GFAP promoter, 2. a Cre-shSCR vector which expressed Cre under the same GFAP promoter and also expressed a scrambled shRNA under a separate U6 promoter (AAV-GFAP-Cre-shSCR), and 3. a Cre-shBag3 vector that expressed GFAP-Cre as well as a *Bag3* shRNA (AAV-GFAP-Cre-shBag3). One month after viral vector injection into the striatum, we injected FITC-labeled tau fibrils into the exact same location, then waited 12 days to assess clearance of this fluorescent tau (Fig. 7a). When comparing the contralateral (uninjected) striatum to the ipsilateral side, some increases in GFAP and BAG3 were seen with the control virus (AAV-GFAP-GFP), suggesting that astrocyte activation caused by injection itself can induce some BAG3 expression (Supplemental Fig. 7a). When examining the ipsilateral striatum, both Cre-expressing viral vectors caused widespread loss of BMAL1 immunoreactivity, though this did not appear to be restricted to astrocytes as was originally intended (Supplemental Fig. 7b). Both Cre-expressing vectors (shSCR and shBag3) caused marked increases in local expression of GFAP as compared to the GFP control vector (Fig. 7b). The AAV-Cre-shSCR vector caused significant increases in BAG3 expression as compared to AAV-GFAP-GFP control, while BAG3 expression was not significantly increased in the AAV-GFAP-Cre-shBag3 group (Fig. 7b). The AAV-GFAP-Cre-shSCR group did not significantly decrease in FITC-tau signal as compared to the control AAV-GFAP-GFAP group, most likely due to this induction of GFAP and BAG3 in the AAV-GFAP-GFP group by the injection itself. However, the AAV-Cre-shBag3-injected mice had significantly more tau remaining than the AAV-GFAP-Cre-shSCR group (Fig. 7b), suggesting that inhibition of BAG3 expression abrogates the clearance of tau in the setting of *Bmal1* deletion.

To determine if astrocyte-restricted *Bag3* overexpression alone could promote protein aggregate clearance in vivo, we injected the AAV-GFAP-Bag3 vector or AAV-GFAP-GFP control vector from Fig. 6j into the ventricles of day P0 mice to induce widespread astrocyte BAG3 overexpression throughout the brain. At 2 month old, we performed the same α Syn PFF injections as in previous experiments, and examined pSyn pathology at 5 months old (Fig. 7c). BAG3 protein was significantly induced throughout the brain, including the cerebral cortex, and co-localized with GFAP staining (Fig. 7d). Astrocyte BAG3 overexpression significantly reduced pSyn pathology in certain brain regions, particularly in the piriform cortex, suggesting an effect on α Syn spreading (Fig. 7e). Levels of pSyn pathology were unchanged in somatosensory cortex and were trending downward in amygdala in mice with Bag3 overexpression, perhaps due to anatomical variability in viral expression (Supplemental Fig. 7c). Taken together with the in vitro experiments in Fig. 6, our data strongly support BAG3 as a mediator of tau and α Syn clearance in *Bmal1*-deficient astrocytes and implicate astrocyte BAG3 expression as a more general mechanism for glial clearance of protein aggregates.

BAG3 is expressed in disease-associated astrocytes in human Alzheimer's Disease.

We next sought to characterize *BAG3* gene expression in astrocytes in human AD, as only a single paper describes astrocyte *BAG3* staining in post-mortem human AD and PD brain²⁹. We first examined the expression of *BAG3* transcript in post-mortem bulk brain tissue from participants across multiple large AD brain banks. We used a random effects model to compare *BAG3* mRNA levels in pathologically-confirmed AD vs. control samples from Mayo Clinic, Rush ROSMAP, Washington University Knight ADRC, and Mount Sinai Brain Bank, encompassing more than 600 total participants. Demographic information for these cohorts is summarized in Supplemental Fig. 8a. *BAG3* expression was higher in AD in all cohorts and was significantly increased by nearly 50% in aggregate (Fig. 8a). When examining *BAG3* expression data more closely in data from the Mount Sinai brain bank³⁰, we observed that *BAG3* was only upregulated in people with symptomatic dementia but not preclinical AD, suggesting that *BAG3* expression occurs later in the disease course (Fig. 8b). To determine the cellular expression of *BAG3* in the human brain, we examined single nucleus RNAseq (snRNAseq) data from the Seattle AD Brain Cell Atlas. We confirmed that the defined astrocyte cluster expressed high levels of *GFAP* and *AQP4*, two astrocyte-enriched genes. *BAG3* expression closely resembled that of *GFAP* and was enriched in the astrocyte cluster, with some additional expression in microglial and endothelial cell clusters (Fig. 8c). To examine the effect of disease on astrocytic *BAG3* expression in humans, we analyzed data from a snRNAseq dataset that includes autosomal dominant AD (ADAD), sporadic AD, and neuropathology-free controls³¹ (Fig. 8d). First, we identified the astrocyte cluster in this dataset and were able to divide this group into five distinct subclusters (Fig. 8d). We identified a homeostatic GFAP-low (Astro.0) subcluster which expressed homeostatic transcripts (*ALDH1L1*, *SLC7A10*, *MFGE8*); a reactive subcluster with high expression *GFAP* and *AQP4* (Astro.1); a subcluster expressing genes related to myelin sheath injury (Astro.2), a subcluster defined by genes related to long term potentiation (Astro.3), and finally a subcluster which resembles the Disease-Associated Astrocytes (DAA) previously described in 5xFAD mice (Astro.4)³² (Fig. 8F). Astro.4 had prominent expression of DAA genes *VIM*, *CTSB*, *OSMR*, and also *BAG3* (Fig. 8d and Supplemental Fig. 8b). When compared directly to homeostatic astrocytes (Astro.0), *BAG3* had the largest fold increase in the DAA-like cluster (Astro.4), followed by Astro.2 (Fig. 8e), suggesting that *BAG3* is expressed in human DAA-like astrocytes in response to disease. A volcano plot of differentially-expressed genes between Astro.0 and Astro.4 is shown in Supplemental Fig. 8c, highlighting several genes upregulated in Astro.4. To understand the timing of astrocyte *BAG3* expression over the course of disease in ADAD patients, we analyzed *BAG3* expression across all Braak stages including all five astrocyte clusters. Here, we found that most astrocyte *BAG3* expression only occurs in the late stages of ADAD (Braak stage 6, Fig 8g). Finally, to extend the relevance of *BAG3* to human PD, we analyzed an existing PD GWAS dataset^{27,33} which describes a SNP in *BAG3* (rs72840788) associated with risk of developing PD (p-value = 2×10^{-11} , Beta; 0.0763-CI=0.054–0.098) (Supplemental Fig 9a). Further analysis using a single nucleus ATAC-seq dataset from the SEA-AD cohort revealed a significant overlap in open chromatin of astrocytes around the rs72840788 SNP (Supplemental Fig. 9b). This suggests that astrocytes could specifically be accessing this region of *BAG3* where a SNP is associated with risk of developing PD. Our analysis of

human data suggests that BAG3 is expressed in reactive, DAA-like astrocytes in the human AD brain, and that SNPs in astrocyte BAG3 may impart risk for developing PD.

DISCUSSION

A persisting question in the field of neurodegeneration is whether astrocyte activation, which is observed almost ubiquitously, is protective or deleterious. Astrocytes are not homogenous, and diverse subpopulations of astrocytes have been described across different neuroanatomical regions^{34–36}, circuits^{37,38}, and disease settings^{34,39–42}. While GFAP has been classically used as a marker of astrocyte reactivity, the transcriptional states and functions of GFAP+ astrocytes can vary immensely depending on context^{2,40}. Transcriptomic profiling studies of astrocytes in neurodegenerative conditions suggest that multiple modes of astrocyte activation exist depending on disease state, some with varying expression of GFAP^{2,13,32,43,44}. Thus, astrocyte reactivity is much more complex than any binary classification^{2,41}. However, the functional consequences of these different activation states in models of AD and PD are not as well understood. Only a few studies have demonstrated that astrocyte-specific manipulations can affect intracellular protein aggregation (such as that seen with tau and α Syn). Constitutive JAK2 activation in astrocytes leads to STAT3 phosphorylation and astrogliosis and was found to reduce intraneuronal huntingtin aggregation by inducing proteasomal activity and expression of the chaperone DNAJB1, though BAG3 was not increased in this model⁴⁴. Conversely, deletion of the astrocytic $\alpha 2$ Na⁺/K⁺-ATPase suppressed astrogliosis and prevented tauopathy in P301S mice⁴⁵. Tauopathy induced NRF2-mediated responses in astrocytes, and *Nrf2* overexpression in astrocytes mitigated tau pathology¹³. Notably, upstream transcription factor analysis of the reactive astrocytes in this study identified BMAL1 (*Arntl*) as a likely regulator of astrocyte transcriptional responses to A β and tau, though the study focused on NRF2. Several studies show that BMAL1 can modulate NRF2 activity and downstream gene expression^{3,46,47}, suggesting that these two transcription factors may interact to mediate protective astrocyte responses to protein aggregation. Our current and previous findings^{4,7,48} suggest that *Bmal1* deletion induces a distinct form of astrocyte reactivity which encompasses robust GFAP expression and classic morphological changes, but with induction of a unique transcriptional signature. This form of astrocyte activation has minimal impact on amyloid plaque formation in APP/PS1 mice⁷, but is protective against tau and α Syn pathology, suggesting that astrocyte activation due to *Bmal1* deletion induces specific cellular adaptations that suppress intraneuronal tau and α Syn aggregation, but not extracellular amyloid-beta deposition. While we have identified BAG3 as a downstream mediator of this phenotype, *Bmal1* deletion alters the expression of many other genes in astrocytes which may contribute to this neuroprotective phenotype⁷, and the function of these genes in the context of disease is an area for future study.

Although tau and α Syn form intra-neuronal aggregates, proteopathic seeding occurs via transmission from cell to cell^{10,21}. Astrocytes can readily take up and degrade α Syn released from neurons in vitro⁴⁹. In *Drosophila*, glia are intermediaries in the neuron-to-neuron transfer of huntingtin species¹¹. Tau aggregates also spread from neurons to astrocytes in vivo in mice⁵⁰, allowing astrocytes to degrade proteopathic species and suppress pathological spreading. We hypothesize that *Bmal1*-deficient astrocytes directly

phagocytose proteopathic species released from neurons and degrade them in a BAG3-dependent manner. Our finding that *Bmal1* gKO mice are not protected from direct seeding of the SNpc (Supplemental Fig. 2e) but do show mitigation of spreading to regions such as cortex (Fig. 3c) suggests that *Bmal1*-deficient astrocytes may interrupt spreading at certain synapses. Alternatively, it remains possible that *Bmal1* KO astrocytes indirectly promote the degradation of protein aggregates by neurons, perhaps by providing chaperone proteins to neurons via exosomes⁴⁴. Further investigation of the specific mechanisms by which astrocytes influence intraneuronal protein aggregation, seeding, and spreading is needed.

Another question stemming from our findings is whether the observed effects of astrocytic *Bmal1* deletion are related to the disruption of circadian rhythms. Astrocyte BMAL1 can regulate the expression of non-rhythmic transcripts⁴⁸, and BMAL1 exerts some cellular functions that are not related to circadian rhythmicity⁵¹. In this case, the effect of *Bmal1* deletion on astrocyte activation is unlikely to be tied to rhythms, as our aKO mice have preserved circadian rhythms of behavior. However, it remains possible that loss of the cell-intrinsic transcriptional rhythms within astrocytes causes chronic cellular adaptations that lead to astrocyte activation and *Bag3* expression. Future studies will be needed to determine how other clock gene mutations or non-genetic circadian disruptions impact tauopathy and α Syn pathology. Regardless of the role of circadian rhythms, our work identifies BMAL1 as a key regulator of neuroprotective astrocyte activation, and reveals BMAL1 and its downstream pathways in astrocytes, including BAG3, as novel neuroprotective therapeutic targets.

Our study has some limitations that merit future consideration. Due to concerns that *Bmal1* deletion might accelerate the pathology (and death) of P301S mice, the experiments with this model were not designed to examine behavior. It is notable that the α -Syn PFF model exhibits very modest behavioral deficits, even at six months post-injection⁵², so a different model or longer timeline might be needed to address behavior. Moreover, *Bmal1* deletion does not prevent direct seeding of the SNpc after striatal PFF injection, and this pathology drives motor behavioral changes in the model. Finally, *Bmal1* KO mice have behavioral abnormalities at baseline, complicating the interpretation of behavioral data in the disease setting³. Another issue was that in Fig. 7, both viral Cre and shRNA expression was not astrocyte-specific. However, since we have shown that global *Bmal1* deletion induces BAG3 specifically in astrocytes, the effects of the *Bag3* shRNA were likely due to the suppression of astrocyte BAG3. Despite these shortcomings, it is well established that tau and α Syn aggregation are critical pathogenic steps in multiple neurodegenerative diseases. Thus, mechanisms by which astrocytes might reduce these pathologies, such as the BMAL1-BAG3 axis described here, have clear translational relevance.

While it may seem surprising that global *Bmal1* deletion, which disrupts circadian rhythms, can exert protective effects in our tau and α Syn mouse models, other studies show protective effects of *Bmal1* deletion in neurological disease^{53–55}. In *Drosophila*, circadian clock disruption (not though *Bmal1* deletion specifically) mitigates neuronal huntingtin aggregation via heat shock protein induction⁵⁶. Conversely, we have previously shown that global or brain-specific *Bmal1* deletion causes spontaneous synaptic loss and oxidative stress in mouse brain³, and can accelerate amyloid plaque deposition in APP/PS1 transgenic

mice⁸. In general, it appears that loss of *Bmal1* in neurons is detrimental, leading not only to circadian arrhythmicity but also direct neurotoxic effects. However, *Bmal1* deletion in astrocytes exerts protective effects in our tau and α Syn models by promoting misfolded protein degradation. Thus, we may be observing opposing effects of global *Bmal1* deletion on protein aggregation and neuronal health, which may be why gKO;P301S mice had similar levels of neuronal loss as P301S mice, despite decreased tau aggregation and inflammation (Fig. 1, 2). Thus, global BMAL1 inhibition in general may not be a viable therapeutic target. However, we hypothesize that downstream pathways activated in *Bmal1*-deficient astrocytes may offer novel targets, such as BAG3. Neuronal BAG3 can facilitate degradation of α Syn and tau aggregates^{23–26}. The effect of astrocyte BAG3 on protein aggregation has not been previously studied, though astrocytic expression of BAG3 and its partner protein HSPB8 has been described by immunohistochemistry in post-mortem AD and PD brain²⁹. Our finding that *Bag3* overexpression in astrocytes can mitigate tau and α Syn pathology, coupled with the clear increases in *BAG3* expression in subclusters of activated astrocytes in humans with AD, suggests that BAG3+ disease-associated astrocytes may be attempting to clear protein aggregates. This attempt is insufficient to prevent disease, perhaps because it occurs too late in the disease course, as we showed that *BAG3* is only increased in symptomatic AD, and that astrocyte activation via *Bmal1* deletion is most protective before protein aggregation (Fig. 5c) Thus, therapies designed to induce protective astrocyte activation early in disease pathogenesis via manipulation of BMAL1 or its downstream target BAG3 may be advantageous for preventing AD and other neurodegenerative diseases.

STAR METHODS

RESOURCE AVAILABILITY

Lead contact: Further information and requests for resources and reagents should be directed to and will be fulfilled by the lead contact, Erik Musiek (musieke@wustl.edu).

Materials availability: Mouse lines used in this study are all publicly available from Jackson Labs. Specific mouse catalog numbers are listed in the Key Resources Table. Specific mouse crosses will also be shared directly by the Musiek Lab.

Viral vectors generated for this study are available from the Musiek Lab, or can be purchased from VectorBuilder (all Php.eb vectors), or the Hope Center Viral Vector Core at Washington University (*Bag3* overexpression vector).

Data and code availability: This paper analyzes existing, publicly available data. These accession numbers for the datasets are listed in the key resources table

This paper does not report original code.

Any additional information required to reanalyze the data reported in this paper is available from the lead contact upon request

EXPERIMENTAL MODEL AND STUDY PARTICIPANT DETAILS

All animal experiments were approved by the Washington University IACUC and were conducted in accordance with AALAC guidelines and under the supervision of the Washington University Department of Comparative Medicine. For P301S experiments, only male mice were used. For other experiments, including PFF injections, mixed-sex cohorts were used as no sex differences have been observed in this model. Mice were group housed in all experiments. *CAG-Cre^{ERT2}*, *Aldh111-Cre^{ERT2}*, *CX3CR1^{ERT2}*, *Bmal1^{flox/flox}*, C57/B6J and *hMAPTP301S PS19 Tg* mice were all obtained from Jackson Labs (Bar Harbor, ME) and crossed in our facility at Washington University in St. Louis. In general, crosses were designed such that *Cre^{+/-};Bmal1^{f/f}* males were bred with *Bmal1^{f/f}* or *Bmal1^{f/f};P301S^{+/-}* females, such that a mix of *Cre⁺* and – littermates were produced for comparison with each other. Litters from several similar breeding cages were combined in each analysis. For experiments with *CAG-Cre^{ERT2}*, *Aldh111-Cre^{ERT2}* lines, all mice (*Cre⁺* and *Cre⁻* littermates) were treated with tamoxifen (3mg/day x 5 days via oral gavage) at 2 months of age. All mice were maintained on a pure C57B6 background except P301S PS19 mice, which are on a mixed C57B6/C3 background. PS19 mice were bred at least 3 generations with C57B6 mice (in order to generate PS19 mice with appropriate *Cre* and floxed alleles), and *Cre⁺* and – littermates were compared in order to account for any remaining background heterogeneity.

METHOD DETAIL

Antibodies: Immunohistochemical antibodies used in this study include: GFAP (rabbit, Dako/Agilent Z0334, 1:5000), IBA1 (goat, Abcam ab5076, 1:500), CD68 (rat, BioRad MCA1957, 1:500), AT8b (mouse, ThermoFisher MN1020, 1:500), GFAP conjugated to Alexafluor-647 (mouse, Cell Signalling Technologies, 3657S, 1:1000), Bmal1 (rabbit, Novus NB100-2288, 1:2000), MC1 (gift of Dr. Peter Davies, 1:500), BAG3 (rabbit, proteintech 10599-1-AP, 1:500), biotinylated phospho-alpha-synuclein (mouse, Biologend 825704, 1:1000).

Immunohistochemistry and imaging: Mice were deeply anesthetized with i.p. pentobarbital (150mg/kg), then perfused with ice-cold Dulbecco's modified PBS (DPBS) containing 3 g/l heparin. For all analyses in the P301S mice; one hemisphere was dissected into regions, flash frozen, and stored at –80o C for RNA analysis as described below. The other hemisphere was post-fixed in 4% paraformaldehyde for 24 hours (4°C), then cryoprotected with 30% sucrose in PBS (4°C) for 24 hours. For all analyses with PFF-injected mice, the whole brain was collected, and fixed in 4% paraformaldehyde for 48 hours (4°C), then cryoprotected with 30% sucrose for 48 hours (4°C). Brains were then sectioned on a freezing sliding microtome in 40-micron serial coronal sections and stored in cryoprotectant solution (30% ethylene glycol, 15% sucrose, 15% phosphate buffer in ddH₂O). Sections were washed in TBS x 3, blocked for 60 minutes in TBSX (TBS+ 0.4% Triton X-100) containing 3% donkey serum, and incubated overnight at 4°C in primary antibodies diluted in TBSX containing 1% donkey serum. Sections were then incubated for 1 hour at room temperature in PBSX (or TBSX with 1:1000 donkey fluorescent secondary antibody and mounted on slides using Prolong Gold (Invitrogen P36930). For AT8b staining, sections were washed in TBS x 3, then incubated in 0.3% hydrogen peroxide for 10 minutes.

Sections were washed again in TBS x 3, then blocked in 3% milk diluted in TBS+0.25% Triton X-100 for 30 minutes. Sections were incubated overnight in biotinylated AT8 in TBS + 0.25% Triton X-100 + 1% milk at 4°C. The next day, sections were washed and then developed using ABC Elite (Vector PK-6100) for 60 minutes. Sections were then incubated in 3,3-diaminobenzidine (DAB, Sigma-Aldrich) and dried before coverslipping. ThioS staining: Free-floating sections were washed in TBS x 3, then incubated in 1% Thioflavin-S dissolved in 80% ethanol for 8 minutes. Sections were then rinsed with 80% ethanol for 1 minute x 2, and rinsed with TBS x 3. Sections were then mounted on slides before coverslipping. All fluorescent imaging was done on a Zeiss Axioimager Z2 or a Keyence BZ-X810 microscope. In general, laser intensity and exposure times were selected for each cohort of samples after a survey of the tissue, in order to select appropriate parameters that could then be held constant for all slides in that imaging session. These values varied by antibody, but all sections in a given cohort were imaged under identical conditions at the same magnification.

For standard image analysis of epifluorescent images (such as determination of % area for antibodies such as MC1 or anti-GFAP), TIFF image files were opened using ImageJ and converted to 8-bit greyscale files. Images with the dimmest and brightest intensity of staining, as well as some mid-range examples, were used to determine an appropriate threshold value that could optimally capture the intended staining across all conditions in that cohort, based on the judgment of the investigator. That threshold was then held constant across all images in the cohort, and black and white images of selected regions of interest were generated and quantified as % area stained using the Analyze Particles function. At least 2 adjacent sections per mouse per region were analyzed and averaged.

Microglia branching analysis was done by taking 20x confocal images of microglia, isolating individual microglia in each image, then the images were binarized and skeletonized using the ImageJ skeletonize plugin. The particle analysis function was then used to remove background before using the Analyze Skeleton function in ImageJ to analyze the number of branches per cell⁵⁷. All branching analysis were done blinded to genotype. All confocal microscopy was performed on a Zeiss LSM700 at 20x magnification. Sections stained with DAB were imaged on the NanoZoomer digital pathology system. Confocal images were analyzed in Imaris where 3D reconstructions were made and volume measurements were calculated.

Tau ELISA: Human tau ELISAs were performed by first fractionating tissue samples. Cortical brain tissue was weighed and RAB buffer (0.1M MES, 0.5mM MgSO₄, 1mM EGTA, 2mM DTT, 0.75M NaCl, protease/phosphatase inhibitors), pH 6.8 was added at 15ul per mg of tissue. Tissue was sonicated at 30% amplitude in pulses for 1 minute. Volumes in each tube were standardized and spun in an ultracentrifuge for 20 min at 50,000xg at 4°C. We then removed the supernatant and stored as RAB fraction. The same volume of RIPA buffer (150mM NaCl, 50mM Tris, 0.5% C₂₄H₃₉O₄Na, 1% Triton-100, 0.5% SDS, 25mM EDTA, protease/phosphatase inhibitors), pH 8.0, was added to the pellet. Samples were then sonicated and run in the ultracentrifuge as before. Supernatant was saved as the RIPA fraction. Formic acid was added at 1/3 of the volume used for RAB and RIPA before being triturated thoroughly and then run once again in the ultracentrifuge before

taking the supernatant as the formic acid fraction. To run the human tau ELISA, plates were coated with 20ug/mL of Tau5 (gift from the Holtzman lab) overnight at 4°C. Plates were washed 5x with PBS then blocked with 4% BSA (Fisher BP9700100) in PBS for an hour at 37°C. Plates were washed 5x before adding diluted sample and tau standard (a gift from the Holtzman lab) in sample buffer (0.25% BSA in PBS, 300mM Tris pH 7.4, phosphatase inhibitor), then incubating overnight at 4°C. Formic acid samples were neutralized by diluting 1:20 in 1M Tris, pH 11.0. Plates were washed 8x with PBS before adding biotinylated HT7 at 0.2ug/mL diluted in 1% BSA+PBS and incubated for 1.5 hours at 37°C. Plates were washed 8x with PBS, then streptavidin poly-HRP40 (Fitzgerald 65R-S104PHRP) diluted 1:4000 in 1% BSA in PBS was added for 1.5 hours. Plates were washed once more before adding super slow TMB substrate (Fisher T5569) and reading absorbance 15 minutes later.

RNA quantification: Brain tissue was homogenized in 500ul of Trizol with beads added before running in a bullet blender for 3 minutes. Cultured cells were collected and homogenized by adding 500ul TRIzol/well of a 12-well plate directly to plated cells. TRIzol samples were then subjected to chloroform extraction (1:6 chloroform:TRIZol, followed by thorough mixing, and centrifugation at 12500 x g for 15 minutes). RNA was then extracted from the aqueous layer using the PureLink RNA Mini Kit according to manufacturer's instructions. RNA concentration was measured on a Nanodrop spectrophotometer, then cDNA was made using a high-capacity RNA-cDNA reverse transcription kit (Applied Biosystems/Life Technologies) with 250ng-1 µg RNA per 20µL reaction. Real-time quantitative PCR was performed with ABI TaqMan primers and ABI PCR Master Mix buffer on ABI StepOnePlus or QuantStudio 12k thermocyclers. Taqman primers (Life Technologies) were used, and mRNA measurements were normalized to β-actin (Actb) mRNA for analysis. For larger experiments, microfluidic qPCR array measurements were performed by the Washington University Genome Technology Access Center using a Fluidigm Biomark HD system, again using Taqman primers. RNA sequencing was performed and values normalized as previously described⁷; GEO accession number is GSE227063. Volcano plot was made using Enhanced Volcano R packaged and heatmap was made using the Pretty Heatmap package. GO pathways were generated using Metascape.org.

Primary mouse astrocyte culture: Primary mouse astrocyte cultures were prepared as previously described⁴. Briefly, P2 mouse pups brains were isolated in cold DMEM, the meninges removed, and the cortices dissected. Cortices were then incubated in 0.025% trypsin solution (Gibco) at 37°C for 15 minutes, then triturated using a glass pipet before adding to a T75 flask. Once cells reached confluency, cells were plated in 24 well plates coated with poly-d-lysine at 70,000 cells per well.

Stereotactic injections: Mice were anesthetized with isoflurane and stereotactically injected with 2ul (approximately 4ug of PFFs) into the left dorsal striatum using a Hamilton microsyringe attached to a motorized injector (Stoelting). The coordinates used were: 0.2mm anterior, 2.0mm lateral to bregma, and 3.2mm ventral to the surface of the skull. The injection was carried out over a 5 minute period, and the needle was left in place for 5

minutes after the injection before it was carefully withdrawn. The skull burr hole was filled with bone wax and the skin sutured.

siRNA transfections: Primary mouse astrocyte-enriched cultures were transfected with siRNA using lipofectamine RNAiMAX (Life Technologies) in Optimem (Life Technologies) per manufacturer's instructions 24–48 hours after replating. 48 hours after transfection, media was changed to DMEM plus 10% FBS and 1% penicillin/streptomycin. SiRNAs targeting mouse Bmal1, Bag3 and Scr (non-targeting, targeting no known mouse gene) were obtained from Horizon Discovery/Dharmacon (Lafayette, CO). ON-TARGETplus SmartPool siRNA was used, which contains 5 separate siRNAs targeting the gene of interest which are pooled together, Bmal1 (product L040483-01-005), non-targeting (control or “scrambled”) (D-001210-01-05), and Bag3 (product L-064450-00-0005). An siRNA:RNAiMAX ratio of 1:1.25) was used, and 40 pmol of siRNA (2uL of 20uM stock) was added to each well in a 24-well plate for 24 hours before replacing with astrocyte media.

Viral vectors: Bag3 overexpression viral vector was made at the Hope Center Viral Vector core using Mammalian Gene Collection cDNA for mouse BAG3 (Enzrez ID 29810) purchased from Horizon Discovery (Lafayette, CO; Cat #: MMM1013-211692359). Bag3 cDNA was then packaged into an AAV8 envelope under expression of a full-length Gfap promoter. An HA tag was also included as a marker of Bag3 expression. These viruses were administered via bilateral intracerebroventricular injection in newborn P0 pups as described previously⁵⁸. Two microliters of virus were injected at a concentration of 8.5×10^{12} gc/mL.

AAV-GFAP-GFP, AAV-GFAP-Cre-shScr, and AAV-GFAP-Cre-shBag3 viral vectors were made by VectorBuilder Inc (Chicago, IL). These employed a Phe.eb capsid (but were injected intracranially, as intravenous injection provided poor density of infection) and used the truncated gfaABC1D promoter to drive either eGFP or Cre recombinase expression primarily in astrocytes. The AAV-GFAP-Cre-shScr, and AAV-GFAP-Cre-shBag3 vectors also contained a separate U6 promoter driving a scrambled, non-targeted shRNA (shSCR), or a shRNA targeting Bag3 (shBag3). The U6 promoter is not cell type-specific, so shRNA expression occurred in all infected cells. Viruses were administered via stereotactic injection, with 2 microliters per injection containing 5×10^{12} gc/mL.

Phagocytosis Assay: Confluent astrocytes were plated at 70,000 cells per well in a 24 well plate. The next day, siRNA was added and then removed the following day. For viral expression, virus was added at 1×10^{11} GC/mL. Three days after addition of virus or siRNA, phrodo-PFFs were added at 2.5ug/mL in astrocyte media for three hours. Cells were then washed once with 1x PBS, and astrocyte media was added back to the cells. 24 hours after phrodo-PFFs were removed, cells were trypsinized, washed twice with flow buffer, then resuspended and analyzed on a MACSQuant VYB flow cytometer. Data was then analyzed in FlowJo software (BD Biosciences).

α Syn PFF preparation and injection: Purification of recombinant mouse sequence α Syn monomer and in vitro fibril assembly were performed as described⁵⁹ with minor modifications. Fibril assembly reactions were carried out in an Eppendorf ThermoMixer at

1000 rpm for 7 days. An aliquot of the resulting suspension was centrifuged at 15,000g for 20 min, and the PFF concentration was estimated by subtracting the concentration of α Syn monomer in the resulting supernatant from the starting monomer concentration. PFFs were aliquoted and stored at -80°C until use. Before use, aliquots were thawed and sonicated briefly in a water bath sonicator (Qsonica). To generate α Syn PFFs conjugated to pHrodo Red, α Syn monomer was labeled with pHrodo Red (ThermoFisher) using a succinimidyl ester reagent (ThermoFisher P36600) according to the manufacturer's instructions, and α Syn PFFs were prepared as above using an excess of unlabeled monomer at a molar ratio of 1:20.

FITC-tau injection study: Fluorescein (FITC)-labeled Tau 441 peptide (rPeptide) was diluted with 10mM 1,4-Dithiothreitol (DTT), 100mM NaCl, and 10mM HEPES and incubated for 1hr at room temperature. Heparin was added at a final concentration of 8 μM , and the solution was incubated with shaking at 37°C for 7 days. Tau solution was then centrifugation at 100,000g for 1 hr at 4°C , and the pellet (containing aggregated tau) was sonicated with 65% power/amplitude for 30 sec in a water bath sonicator, then diluted for use. FITC-tau fibrils (500ng in 1.5uL volume) were injected into the striatum of *Bmal1^{f/f}* one month after viral vector injection at the same coordinates (see above). 12 days after tau injection, mice were perfused and remaining FITC-tau signal was quantified. Serial striatal sections 40 μm apart were imaged, and the section at the epicenter of injection was identified for each mouse by visualization of the needle tract. 3 sections centered on the injection site were then analyzed for FITC signal, for a total area spanning 40 μm on either side (rostral and caudal) of the injection. The harmonic mean of the FITC-Tau percent area in the 3 sections was obtained to mitigate the potential outlier effect of the section closest to the injection site.

Human RNAseq analysis: This manuscript used existing, publicly available and GEO numbers are listed in the Key Resources Table. Bulk RNAseq data from *Aldh111-Cre^{ERT2}*, *Bmal1^{f/f}* mice and Cre- controls has been deposited at GEO and is publicly available. The GEO accession number is listed in the Key Resources Table. Human brain microarray data was previously published and is publicly available in GEO, and was analyzed using the online GEO2r tool. Human single nucleus RNAseq data is also publicly available from the Seattle Alzheimer's Disease Brain Cell Atlas (<https://portal.brain-map.org/explore/seattle-alzheimers-disease>) and was analyzed using the online Transcriptomics Comparative Viewer tool. Single nucleus RNAseq data from autosomal-dominant AD patients was from a previously-published manuscript³¹ and is publicly available online (<http://ngi.pub/SNARE/browse/>) and through the NIAGADS website (<https://dss.niagads.org/datasets/ng00108/>).

All RNA-seq datasets were processed and aligned using our in-house RNA-seq pipeline (<https://github.com/HarariLab/RNA-seq-Pipeline>). Genome reference and gene models were selected similarly to the TOPmed pipeline (https://github.com/broadinstitute/gtex-pipeline/blob/master/TOPMed_RNAseq_pipeline.md). Reference genome GRCh38 and GENCODE 33 annotation, including the addition of ERCC spike-in annotations, were used. Before alignment, the quality of raw read sequences for all libraries was assessed using

FastQC (v0.11.9)¹⁵⁰. All raw read sequences were aligned to the human reference genome (GRCh38) using STAR (v.2.7.1a)¹⁵¹. The alignment quality was evaluated using sequencing metrics such as reads distribution, ribosomal content, or alignment quality provided by STAR using tools (v.2.8.2)¹⁵². All samples that failed to pass the QC or were outliers were removed from the downstream analyses. Raw read counts for transcripts and genes were generated using STAR and computed transcript/gene expression levels as normalized in FPKM (Fragments Per Kilobase of transcript per Million mapped reads) format.

Single-nucleus gene expression and ATAC-seq data from aged controls and sporadic AD patients (Fig. 8c) were obtained from the Seattle AD Brain Cell atlas (<https://portal.brain-map.org/explore/seattle-alzheimers-disease>), which is part of the Allen Brain Map. Genes of interest were queried directly in their web-based Transcriptomic Comparative viewer. Images were taken directly from this viewer, using the SEA-AD cohort, which includes log-normalized expression of each transcript of interest across all nucleus clusters from 84 aged individuals (42 cognitively-normal and 42 with dementia).

Single-nucleus RNAseq data from autosomal dominant AD patients and healthy controls were obtained from frozen parietal cortex of postmortem brains from the Neuropathology Cores of the Charles F. and Joanne Knight Alzheimer's Disease Research Center (Knight-ADRC) and the Dominantly Inherited Alzheimer Network (DIAN). These samples were obtained with informed consent for research use and were approved by the review board of Washington University in St. Louis. AD neuropathological changes were assessed according to the criteria of the National Institute on Aging-Alzheimer's Association (NIA-AA). Their demographic, clinical severity and neuropathological information are presented in Brase L et al.³¹ Nuclei were extracted from fresh frozen brain regions (~200–400mg of tissue) following the same protocol, as reported in Del Aguila et al⁶⁰ and Benitez BA ([dx.doi.org/10.17504/protocols.io.2a5gag6](https://doi.org/10.17504/protocols.io.2a5gag6)). 10X genomic library preparation: Nuclei were processed using the 10x Genomics Chromium Controller and the Chromium Next Gem Single Cell 10× 3' Library & Gel Bead Kit v3.1 (PN 1000121) following the standard manufacturer's protocols (10X Genomics). Samples were sequenced on the Illumina NovaSeq S4 (200 cycles), targeting 50,000 reads/cell (2 × 150 paired-end reads). Sequencing alignment: We employed the 10X Cell Ranger 6.0 pipeline to perform transcript alignment (human genome build GRCh38), counting, and inter-library normalization. Quality control for nucleus inclusion: We followed the Seurat v4 protocol to clean the snRNA-seq data. Each raw gene expression matrix for each sample was plotted using BarcodeInflectionsPlot to calculate the inflection points derived from the barcode-rank distribution. Once the thresholds were determined, a subset of the data was isolated. We removed nuclei with high mitochondria gene expression following a previously proposed dynamic model. Briefly, the nuclei were grouped by their percentage of mitochondria values using k = 2 clusterings, and the group with the higher percentage values was removed. Genes that were not expressed in at least ten nuclei were removed from the final matrix. To detect and discard doublets, we used Doublet Finder, which removes nuclei with expression profiles that resemble synthetically mixed nuclei from the dataset. The gene expression matrices from all samples were combined in R for further processing using the Seurat protocol. The expression matrix was normalized using the SCTransform protocol by Seurat.

We regressed, during the normalization, against the number of Genes, number of UMI, and the percentage of mitochondria. The principal components (PC) were calculated using the first 3,000 variable genes and the Uniform Manifold Approximation and Projection (UMAP) analysis was performed with the top 14 PCs. Clustering and visualization: We clustered nuclei using a graph-based clustering approach implemented in the Seurat package (v4). Cell-type annotation and sub-clustering: For each pre-cluster, we will assign a major brain cell-type label evaluating the enrichment for sets of marker genes for neurons, astrocytes, oligodendrocytes, microglia, oligodendrocyte precursor cells, and endothelial cells, as we previously published (Brase et al). We employed the following markers RYR3, LRR16A, F3, ETNPPL, CLU, SLC1A2, GJA1, DIO2, SLC4A4, EDNRB, AQP4, GPR37L1, CPE, ATP1B2 and SLCO1C1 for astrocytes. Cell-type/-subtype differentially expressed genes (DEG): We identified sub-cluster up/down expressed genes for each cell type to characterize the genes, pathways, and biological processes. We used traditional regression methods (Monocle3 package). We then employed Seurat's FindNeighbors and FindClusters functions to identify unique cell states or subclusters (resolution=0.1, 0.2, 0.2, 0.05, 0.15). Additionally, we used the Garnett protocol to examine nuclei in each expression state within each cell type to detect and remove those nuclei that did not resemble a trustworthy expression profile from downstream analyses.

For RNA-seq harmonization and BAG3 expression quantification in AD brain cohorts, frozen postmortem parietal lobe tissue samples from Knight Alzheimer Disease Research Center (Knight ADRC) participants, collected with informed consent for research use, were provided by the Knight ADRC Neuropathology Core. The data generation for the RNA-seq dataset has been previously described³¹. The data is found at the National Institute on Aging Genetics of Alzheimer's Disease Data Storage Site: NG00083. The RNA-seq raw data from The Mount Sinai Brain Bank (MSBB: syn3157743), the Religious Orders Study and Memory and Aging Project (ROSMAP; syn3219045), and the Mayo Clinic Brain Bank RNA-seq (Mayo; syn5550404) studies were downloaded from the Synapse portal as part of the Accelerating Medicines Partnership for Alzheimer's Disease (AMP-AD).

Data from gene expression from control, presymptomatic (preclinical) and symptomatic AD was from a previously-published study³⁰ and accessed via the GEO database accession number GSE84422. Data from parahippocampal gyrus (PHG) was analyzed. We performed the comparisons using the GEO2R web tool from NCBI (<https://www.ncbi.nlm.nih.gov/geo/geo2r/>).

QUANTIFICATION AND STATISTICAL ANALYSIS

Statistics: In all figures, graphs depict the mean \pm SEM, and N generally indicates the number of animals, unless otherwise noted in the figure legend. For cell culture experiment, each datapoint depicts the mean for several technical replicates from one independent experiment, and each of these mean values is considered an N or 1. An F test was first performed for datasets with a single dependent variable and 2 groups, to determine if variances were significantly different. If not, 2-tailed unpaired T-test was performed. If variances were different, non-parametric Mann-Whitney U test was performed. For datasets with one dependent variable and more than 2 groups, one-way ANOVA was performed.

If the main effect was significant, then Tukey (for equal group sizes) or Tukey-Kramer (for unequal group sizes) multiple comparisons test were subsequently performed. When data was not normally distributed, Kruskal-Wallis test was performed with Dunn's Multiple Comparison test to follow (if main effect was significant). For datasets with 2 dependent variables, 2-way ANOVA was performed, and if main effect was significant, Sidak multiple comparisons test was then added for appropriate sets of variables. Outliers were identified using Grubbs test and were excluded. Statistical tests were performed with GraphPad Prism software, version 9.0.1. P values greater than 0.1 were noted as not significant (NS), while P values from 0.1–0.05 were specifically listed in the figure. $P < 0.05$ was considered significant and was noted with asterisks indicated the p-value: * $P < 0.05$, ** < 0.01 , *** < 0.005 , **** < 0.0001 .

Supplementary Material

Refer to Web version on PubMed Central for supplementary material.

Acknowledgements

This work was supported by NIH grants R01AG054517 and RF1AG061776 (ESM); K08NS101118 (AAD), the Mary E. Groff Charitable Trust, and the Dobbins Family Fund (AAD); R01NS118146, R21NS127211, and RF1AG071706 (BAB); R01AG057777, R56AG067764 and U01 AG072464 (OH) and support from Knight ADRC (P30AG066444; P01AGO26276), and the Dominantly inherited Alzheimer Network (U19AG032438). OH is an Archer Foundation Research Scientist. PWS and LB were supported by NIA grant T32AG058518 through the Knight ADRC. The Genome Technology Access Center (GTAC) is partially supported by NCI grant P30 CA91842, ICTS/CTSA grant# UL1TR002345, and NIH Roadmap for Medical Research. Human data was obtained from AD Knowledge Portal (<https://adknowledgeportal.org>), which is fully acknowledged in Table S1, and the Seattle AD Brain Cell Atlas, which is funded by NIA grant U19AG060909.

References

1. Arranz AM, and De Strooper B (2019). The role of astroglia in Alzheimer's disease: pathophysiology and clinical implications. *Lancet Neurol* 18, 406–414. 10.1016/S1474-4422(18)30490-3. [PubMed: 30795987]
2. Escartin C, Galea E, Lakatos A, O'Callaghan JP, Petzold GC, Serrano-Pozo A, Steinhilber C, Volterra A, Carmignoto G, Agarwal A, et al. (2021). Reactive astrocyte nomenclature, definitions, and future directions. *Nat Neurosci* 24, 312–325. 10.1038/s41593-020-00783-4. [PubMed: 33589835]
3. Musiek ES, Lim MM, Yang G, Bauer AQ, Qi L, Lee Y, Roh JH, Ortiz-Gonzalez X, Dearborn JT, Culver JP, et al. (2013). Circadian clock proteins regulate neuronal redox homeostasis and neurodegeneration. *J Clin Invest* 123, 5389–5400. 10.1172/JCI70317 [PubMed: 24270424]
4. Lananna BV, Nadarajah CJ, Izumo M, Cedeno MR, Xiong DD, Dimitry J, Tso CF, McKee CA, Griffin P, Sheehan PW, et al. (2018). Cell-Autonomous Regulation of Astrocyte Activation by the Circadian Clock Protein BMAL1. *Cell Rep* 25, 1–9 e5. 10.1016/j.celrep.2018.09.015. [PubMed: 30282019]
5. Bunger MK, Wilsbacher LD, Moran SM, Clendenin C, Radcliffe LA, Hogenesch JB, Simon MC, Takahashi JS, and Bradfield CA (2000). Mop3 is an essential component of the master circadian pacemaker in mammals. *Cell* 103, 1009–1017. [PubMed: 11163178]
6. McKee CA, Lananna BV, and Musiek ES (2020). Circadian regulation of astrocyte function: implications for Alzheimer's disease. *Cell Mol Life Sci* 77, 1049–1058. 10.1007/s00018-019-03314-y. [PubMed: 31578625]
7. McKee CA, Lee J, Cai Y, Saito T, Saido T, and Musiek ES (2022). Astrocytes deficient in circadian clock gene *Bmal1* show enhanced activation responses to amyloid-beta pathology without changing plaque burden. *Sci Rep* 12, 1796. 10.1038/s41598-022-05862-z. [PubMed: 35110643]

8. Kress GJ, Liao F, Dimitry J, Cedeno MR, FitzGerald GA, Holtzman DM, and Musiek ES (2018). Regulation of amyloid-beta dynamics and pathology by the circadian clock. *J Exp Med* 215, 1059–1068. 10.1084/jem.20172347 [PubMed: 29382695]
9. Cirrito JR, Yamada KA, Finn MB, Sloviter RS, Bales KR, May PC, Schoepp DD, Paul SM, Mennerick S, and Holtzman DM (2005). Synaptic activity regulates interstitial fluid amyloid-beta levels in vivo. *Neuron* 48, 913–922. 10.1016/j.neuron.2005.10.028. [PubMed: 16364896]
10. Frost B, Jacks RL, and Diamond MI (2009). Propagation of tau misfolding from the outside to the inside of a cell. *J Biol Chem* 284, 12845–12852. 10.1074/jbc.M808759200 [PubMed: 19282288]
11. Donnelly KM, DeLorenzo OR, Zaya AD, Pisano GE, Thu WM, Luo L, Kopito RR, and Panning Pearce MM (2020). Phagocytic glia are obligatory intermediates in transmission of mutant huntingtin aggregates across neuronal synapses. *Elife* 9. 10.7554/eLife.58499.
12. Toledo JB, Cairns NJ, Da X, Chen K, Carter D, Fleisher A, Householder E, Ayutyanont N, Rontiva A, Bauer RJ, et al. (2013). Clinical and multimodal biomarker correlates of ADNI neuropathological findings. *Acta Neuropathol Commun* 1, 65. 10.1186/2051-5960-1-65. [PubMed: 24252435]
13. Jiwaji Z, Tiwari SS, Avilés-Reyes RX, Hooley M, Hampton D, Torvell M, Johnson DA, McQueen J, Baxter P, Sabari-Sankar K, et al. (2022). Reactive astrocytes acquire neuroprotective as well as deleterious signatures in response to Tau and A β pathology. *Nat Commun* 13, 135. 10.1038/s41467-021-27702-w. [PubMed: 35013236]
14. Yang G, Chen L, Grant GR, Paschos G, Song WL, Musiek ES, Lee V, McLoughlin SC, Grosser T, Cotsarelis G, and FitzGerald GA (2016). Timing of expression of the core clock gene *Bmal1* influences its effects on aging and survival. *Sci Transl Med* 8, 324ra316. 10.1126/scitranslmed.aad3305
15. Yoshiyama Y, Higuchi M, Zhang B, Huang SM, Iwata N, Saido TC, Maeda J, Suhara T, Trojanowski JQ, and Lee VM (2007). Synapse loss and microglial activation precede tangles in a P301S tauopathy mouse model. *Neuron* 53, 337–351. 10.1016/j.neuron.2007.01.010. [PubMed: 17270732]
16. Jicha GA, Bowser R, Kazam IG, and Davies P (1997). Alz-50 and MC-1, a new monoclonal antibody raised to paired helical filaments, recognize conformational epitopes on recombinant tau. *J Neurosci Res* 48, 128–132. 10.1002/(sici)1097-4547(19970415)48:2<128::aid-jnr5>3.0.co;2-e. [PubMed: 9130141]
17. Shi Y, Yamada K, Liddelow SA, Smith ST, Zhao L, Luo W, Tsai RM, Spina S, Grinberg LT, Rojas JC, et al. (2017). ApoE4 markedly exacerbates tau-mediated neurodegeneration in a mouse model of tauopathy. *Nature* 549, 523–527. 10.1038/nature24016 [PubMed: 28959956]
18. Keren-Shaul H, Spinrad A, Weiner A, Matcovitch-Natan O, Dvir-Szternfeld R, Ulland TK, David E, Baruch K, Lara-Astaiso D, Toth B, et al. (2017). A Unique Microglia Type Associated with Restricting Development of Alzheimer's Disease. *Cell* 169, 1276–1290 e1217. 10.1016/j.cell.2017.05.018. [PubMed: 28602351]
19. Schafer DP, Lehrman EK, Kautzman AG, Koyama R, Mardinly AR, Yamasaki R, Ransohoff RM, Greenberg ME, Barres BA, and Stevens B (2012). Microglia sculpt postnatal neural circuits in an activity and complement-dependent manner. *Neuron* 74, 691–705. 10.1016/j.neuron.2012.03.026 [PubMed: 22632727]
20. Luk KC, Kehm V, Carroll J, Zhang B, O'Brien P, Trojanowski JQ, and Lee VM (2012). Pathological alpha-synuclein transmission initiates Parkinson-like neurodegeneration in nontransgenic mice. *Science* 338, 949–953. 10.1126/science.1227157. [PubMed: 23161999]
21. Volpicelli-Daley LA, Luk KC, Patel TP, Tanik SA, Riddle DM, Stieber A, Meaney DF, Trojanowski JQ, and Lee VM (2011). Exogenous alpha-synuclein fibrils induce Lewy body pathology leading to synaptic dysfunction and neuron death. *Neuron* 72, 57–71. 10.1016/j.neuron.2011.08.033. [PubMed: 21982369]
22. Srinivasan R, Lu TY, Chai H, Xu J, Huang BS, Golshani P, Coppola G, and Khakh BS (2016). New Transgenic Mouse Lines for Selectively Targeting Astrocytes and Studying Calcium Signals in Astrocyte Processes In Situ and In Vivo. *Neuron* 92, 1181–1195. 10.1016/j.neuron.2016.11.030. [PubMed: 27939582]
23. Lin H, Tang M, Ji C, Girardi P, Cvetojevic G, Chen D, Koren SA, and Johnson GVW (2022). BAG3 Regulation of RAB35 Mediates the Endosomal Sorting Complexes Required

- for Transport/Endolysosome Pathway and Tau Clearance. *Biol Psychiat* 92, 10–24. 10.1016/j.biopsych.2021.10.024. [PubMed: 35000752]
24. Cao YL, Yang YP, Mao CJ, Zhang XQ, Wang CT, Yang J, Lv DJ, Wang F, Hu LF, and Liu CF (2017). A role of BAG3 in regulating SNCA/ α -synuclein clearance via selective macroautophagy. *Neurobiol Aging* 60, 104–115. 10.1016/j.neurobiolaging.2017.08.023. [PubMed: 28941726]
 25. Fu H, Possenti A, Freer R, Nakano Y, Hernandez Villegas NC, Tang M, Cauhy PVM, Lassus BA, Chen S, Fowler SL, et al. (2019). A tau homeostasis signature is linked with the cellular and regional vulnerability of excitatory neurons to tau pathology. *Nat Neurosci* 22, 47–56. 10.1038/s41593-018-0298-7. [PubMed: 30559469]
 26. Ji C, Tang M, Zeidler C, Hohfeld J, and Johnson GV (2019). BAG3 and SYNPO (synaptopodin) facilitate phospho-MAPT/Tau degradation via autophagy in neuronal processes. *Autophagy* 15, 1199–1213. 10.1080/15548627.2019.1580096. [PubMed: 30744518]
 27. Nalls MA, Blauwendraat C, Vallerga CL, Heilbron K, Bandres-Ciga S, Chang D, Tan M, Kia DA, Noyce AJ, Xue A, et al. (2019). Identification of novel risk loci, causal insights, and heritable risk for Parkinson's disease: a meta-analysis of genome-wide association studies. *Lancet Neurol* 18, 1091–1102. 10.1016/s1474-4422(19)30320-5. [PubMed: 31701892]
 28. Colas C, Menezes S, Gutiérrez-Martínez E, Péan CB, Dionne MS, and Guernonprez P (2014). An improved flow cytometry assay to monitor phagosome acidification. *J Immunol Methods* 412, 1–13. 10.1016/j.jim.2014.06.008. [PubMed: 24952246]
 29. Seidel K, Vinet J, Dunnen WF, Brunt ER, Meister M, Boncoraglio A, Zijlstra MP, Boddeke HW, Rüb U, Kampinga HH, and Carra S (2012). The HSPB8-BAG3 chaperone complex is upregulated in astrocytes in the human brain affected by protein aggregation diseases. *Neuropathol Appl Neurobiol* 38, 39–53. 10.1111/j.1365-2990.2011.01198.x. [PubMed: 21696420]
 30. Wang M, Roussos P, McKenzie A, Zhou X, Kajiwara Y, Brennand KJ, De Luca GC, Crary JF, Casaccia P, Buxbaum JD, et al. (2016). Integrative network analysis of nineteen brain regions identifies molecular signatures and networks underlying selective regional vulnerability to Alzheimer's disease. *Genome Med* 8, 104. 10.1186/s13073-016-0355-3. [PubMed: 27799057]
 31. Brase L, You SF, D'Oliveira Albanus R, Del-Aguila JL, Dai Y, Novotny BC, Soriano-Tarraga C, Dykstra T, Fernandez MV, Budde JP, et al. (2023). Single-nucleus RNA-sequencing of autosomal dominant Alzheimer disease and risk variant carriers. *Nat Commun* 14, 2314. 10.1038/s41467-023-37437-5. [PubMed: 37085492]
 32. Habib N, McCabe C, Medina S, Varshavsky M, Kitsberg D, Dvir-Szternfeld R, Green G, Dionne D, Nguyen L, Marshall JL, et al. (2020). Disease-associated astrocytes in Alzheimer's disease and aging. *Nat Neurosci* 23, 701–706. 10.1038/s41593-020-0624-8. [PubMed: 32341542]
 33. Grenn FP, Kim JJ, Makarios MB, Iwaki H, Illarionova A, Brolin K, Kluss JH, Schumacher-Schuh AF, Leonard H, Faghri F, et al. (2020). The Parkinson's Disease Genome-Wide Association Study Locus Browser. *Mov Disord* 35, 2056–2067. 10.1002/mds.28197. [PubMed: 32864809]
 34. John Lin CC, Yu K, Hatcher A, Huang TW, Lee HK, Carlson J, Weston MC, Chen F, Zhang Y, Zhu W, et al. (2017). Identification of diverse astrocyte populations and their malignant analogs. *Nat Neurosci* 20, 396–405. 10.1038/nn.4493. [PubMed: 28166219]
 35. Bayraktar OA, Bartels T, Holmqvist S, Kleshchevnikov V, Martirosyan A, Polioudakis D, Ben Haim L, Young AMH, Batiuk MY, Prakash K, et al. (2020). Astrocyte layers in the mammalian cerebral cortex revealed by a single-cell in situ transcriptomic map. *Nat Neurosci* 23, 500–509. 10.1038/s41593-020-0602-1. [PubMed: 32203496]
 36. Molofsky AV, Kelley KW, Tsai HH, Redmond SA, Chang SM, Madireddy L, Chan JR, Baranzini SE, Ullian EM, and Rowitch DH (2014). Astrocyte-encoded positional cues maintain sensorimotor circuit integrity. *Nature* 509, 189–194. 10.1038/nature13161. [PubMed: 24776795]
 37. Chai H, Diaz-Castro B, Shigetomi E, Monte E, Octeau JC, Yu X, Cohn W, Rajendran PS, Vondriska TM, Whitelegge JP, et al. (2017). Neural Circuit-Specialized Astrocytes: Transcriptomic, Proteomic, Morphological, and Functional Evidence. *Neuron* 95, 531–549.e539. 10.1016/j.neuron.2017.06.029. [PubMed: 28712653]
 38. Huang AY, Woo J, Sardar D, Lozzi B, Bosquez Huerta NA, Lin CJ, Felice D, Jain A, Paulucci-Holthausen A, and Deneen B (2020). Region-Specific Transcriptional Control of Astrocyte Function Oversees Local Circuit Activities. *Neuron* 106, 992–1008.e1009. 10.1016/j.neuron.2020.03.025. [PubMed: 32320644]

39. Molofsky AV, Krencik R, Ullian EM, Tsai HH, Deneen B, Richardson WD, Barres BA, and Rowitch DH (2012). Astrocytes and disease: a neurodevelopmental perspective. *Genes Dev* 26, 891–907. 10.1101/gad.188326.112. [PubMed: 22549954]
40. Sadick JS, O’Dea MR, Hasel P, Dykstra T, Faustin A, and Liddelow SA (2022). Astrocytes and oligodendrocytes undergo subtype-specific transcriptional changes in Alzheimer’s disease. *Neuron* 110, 1788–1805.e1710. 10.1016/j.neuron.2022.03.008. [PubMed: 35381189]
41. Khakh BS, and Deneen B (2019). The Emerging Nature of Astrocyte Diversity. *Annu Rev Neurosci* 42, 187–207. 10.1146/annurev-neuro-070918-050443. [PubMed: 31283899]
42. Laug D, Huang TW, Huerta NAB, Huang AY, Sardar D, Ortiz-Guzman J, Carlson JC, Arenkiel BR, Kuo CT, Mohila CA, et al. (2019). Nuclear factor I-A regulates diverse reactive astrocyte responses after CNS injury. *J Clin Invest* 129, 4408–4418. 10.1172/jci127492. [PubMed: 31498149]
43. Diaz-Castro B, Gangwani MR, Yu X, Coppola G, and Khakh BS (2019). Astrocyte molecular signatures in Huntington’s disease. *Sci Transl Med* 11, eaaw8546. 10.1126/scitranslmed.aaw8546.
44. Abjean L, Ben Haim L, Riquelme-Perez M, Gipchtein P, Derbois C, Palomares MA, Petit F, Hérard AS, Gaillard MC, Guillermier M, et al. (2022). Reactive astrocytes promote proteostasis in Huntington’s disease through the JAK2-STAT3 pathway. *Brain* 146, 149–166. 10.1093/brain/awac068.
45. Mann CN, Devi SS, Kersting CT, Bleem AV, Karch CM, Holtzman DM, and Gallardo G (2022). Astrocytic α 2-Na(+)/K(+) ATPase inhibition suppresses astrocyte reactivity and reduces neurodegeneration in a tauopathy mouse model. *Sci Transl Med* 14, eabm4107. 10.1126/scitranslmed.abm4107.
46. Early JO, Menon D, Wyse CA, Cervantes-Silva MP, Zaslona Z, Carroll RG, Palsson-McDermott EM, Angiari S, Ryan DG, Corcoran SE, et al. (2018). Circadian clock protein BMAL1 regulates IL-1 β in macrophages via NRF2. *Proc Natl Acad Sci USA* 115, E8460–e8468. 10.1073/pnas.1800431115. [PubMed: 30127006]
47. Lee J, Moulik M, Fang Z, Saha P, Zou F, Xu Y, Nelson DL, Ma K, Moore DD, and Yechoor VK (2013). Bmal1 and beta-cell clock are required for adaptation to circadian disruption, and their loss of function leads to oxidative stress-induced beta-cell failure in mice. *Mol Cell Biol* 33, 2327–2338. 10.1128/MCB.01421-12. [PubMed: 23547261]
48. Lananna BV, McKee CA, King MW, Del-Aguila JL, Dimitry JM, Farias FHG, Nadarajah CJ, Xiong DD, Guo C, Cammack AJ, et al. (2020). Chi311/YKL-40 is controlled by the astrocyte circadian clock and regulates neuroinflammation and Alzheimer’s disease pathogenesis. *Sci Transl Med* 12, eaax3519. 10.1126/scitranslmed.aax3519.
49. Loria F, Vargas JY, Bousset L, Syan S, Salles A, Melki R, and Zurzolo C (2017). alpha-Synuclein transfer between neurons and astrocytes indicates that astrocytes play a role in degradation rather than in spreading. *Acta Neuropathol* 134, 789–808. 10.1007/s00401-017-1746-2. [PubMed: 28725967]
50. Maté de Gérando A, d’Orange M, Augustin E, Joséphine C, Aurégan G, Gaudin-Guérif M, Guillermier M, Hérard AS, Stimmer L, Petit F, et al. (2021). Neuronal tau species transfer to astrocytes and induce their loss according to tau aggregation state. *Brain* 144, 1167–1182. 10.1093/brain/awab011. [PubMed: 33842937]
51. Yu EA, and Weaver DR (2011). Disrupting the circadian clock: gene-specific effects on aging, cancer, and other phenotypes. *Aging* 3, 479–493. [PubMed: 21566258]
52. Stoyka LE, Arrant AE, Thrasher DR, Russell DL, Freire J, Mahoney CL, Narayanan A, Dib AG, Standaert DG, and Volpicelli-Daley LA (2020). Behavioral defects associated with amygdala and cortical dysfunction in mice with seeded α -synuclein inclusions. *Neurobiol Dis* 134, 104708. 10.1016/j.nbd.2019.104708. [PubMed: 31837424]
53. Druzd D, Matveeva O, Ince L, Harrison U, He W, Schmal C, Herzel H, Tsang AH, Kawakami N, Leliavski A, et al. (2017). Lymphocyte Circadian Clocks Control Lymph Node Trafficking and Adaptive Immune Responses. *Immunity* 46, 120–132. 10.1016/j.immuni.2016.12.011. [PubMed: 28087238]
54. Sutton CE, Finlay CM, Raverdeau M, Early JO, DeCoursey J, Zaslona Z, O’Neill LAJ, Mills KHG, and Curtis AM (2017). Loss of the molecular clock in myeloid cells exacerbates T

- cell-mediated CNS autoimmune disease. *Nat Commun* 8, 1923. 10.1038/s41467-017-02111-0. [PubMed: 29234010]
55. Slomnicki LP, Myers SA, Saraswat Ohri S, Parsh MV, Andres KR, Chariker JH, Rouchka EC, Whittemore SR, and Hetman M (2020). Improved locomotor recovery after contusive spinal cord injury in *Bmal1(-/-)* mice is associated with protection of the blood spinal cord barrier. *Sci Rep* 10, 14212. 10.1038/s41598-020-71131-6. [PubMed: 32848194]
56. Xu F, Kula-Eversole E, Iwanaszko M, Hutchison AL, Dinner A, and Allada R (2019). Circadian Clocks Function in Concert with Heat Shock Organizing Protein to Modulate Mutant Huntingtin Aggregation and Toxicity. *Cell Rep* 27, 59–70.e54. 10.1016/j.celrep.2019.03.015. [PubMed: 30943415]
57. Filipello F, Morini R, Corradini I, Zerbi V, Canzi A, Michalski B, Erreni M, Markicevic M, Starvaggi-Cucuzza C, Otero K, et al. (2018). The Microglial Innate Immune Receptor TREM2 Is Required for Synapse Elimination and Normal Brain Connectivity. *Immunity* 48, 979–991.e978. 10.1016/j.immuni.2018.04.016. [PubMed: 29752066]
58. Kim JY, Grunke SD, Levites Y, Golde TE, and Jankowsky JL (2014). Intracerebroventricular viral injection of the neonatal mouse brain for persistent and widespread neuronal transduction. *J Vis Exp*, 51863. 10.3791/51863. [PubMed: 25286085]
59. Volpicelli-Daley LA, Luk KC, and Lee VM (2014). Addition of exogenous alpha-synuclein preformed fibrils to primary neuronal cultures to seed recruitment of endogenous alpha-synuclein to Lewy body and Lewy neurite-like aggregates. *Nature protocols* 9, 2135–2146. 10.1038/nprot.2014.143. [PubMed: 25122523]
60. Del-Aguila JL, Li Z, Dube U, Mihindukulasuriya KA, Budde JP, Fernandez MV, Ibanez L, Bradley J, Wang F, Bergmann K, et al. (2019). A single-nuclei RNA sequencing study of Mendelian and sporadic AD in the human brain. *Alzheimers Res Ther* 11, 71. 10.1186/s13195-019-0524-x. [PubMed: 31399126]
61. Love MI, Huber W, Anders S (2014). Moderated estimation of fold change and dispersion for RNA-seq data with DESeq2. *Genome Biology*, 15, 550. 10.1186/s13059-014-0550-8 [PubMed: 25516281]
62. Wickham H (2009) *ggplot2: Elegant Graphics for Data Analysis* (Springer New York, NY)

HIGHLIGHTS

- Global or astrocytic deletion clock gene *Bmal1* reduces tau and α -synuclein pathology.
- Astrocyte *Bmal1* regulates autophagy chaperone *Bag3* to prevent protein aggregation.
- Astrocytic *Bag3* overexpression reduces alpha-synuclein spreading in mice.
- *BAG3* is expressed in disease-associated astrocytes in human Alzheimer Disease.

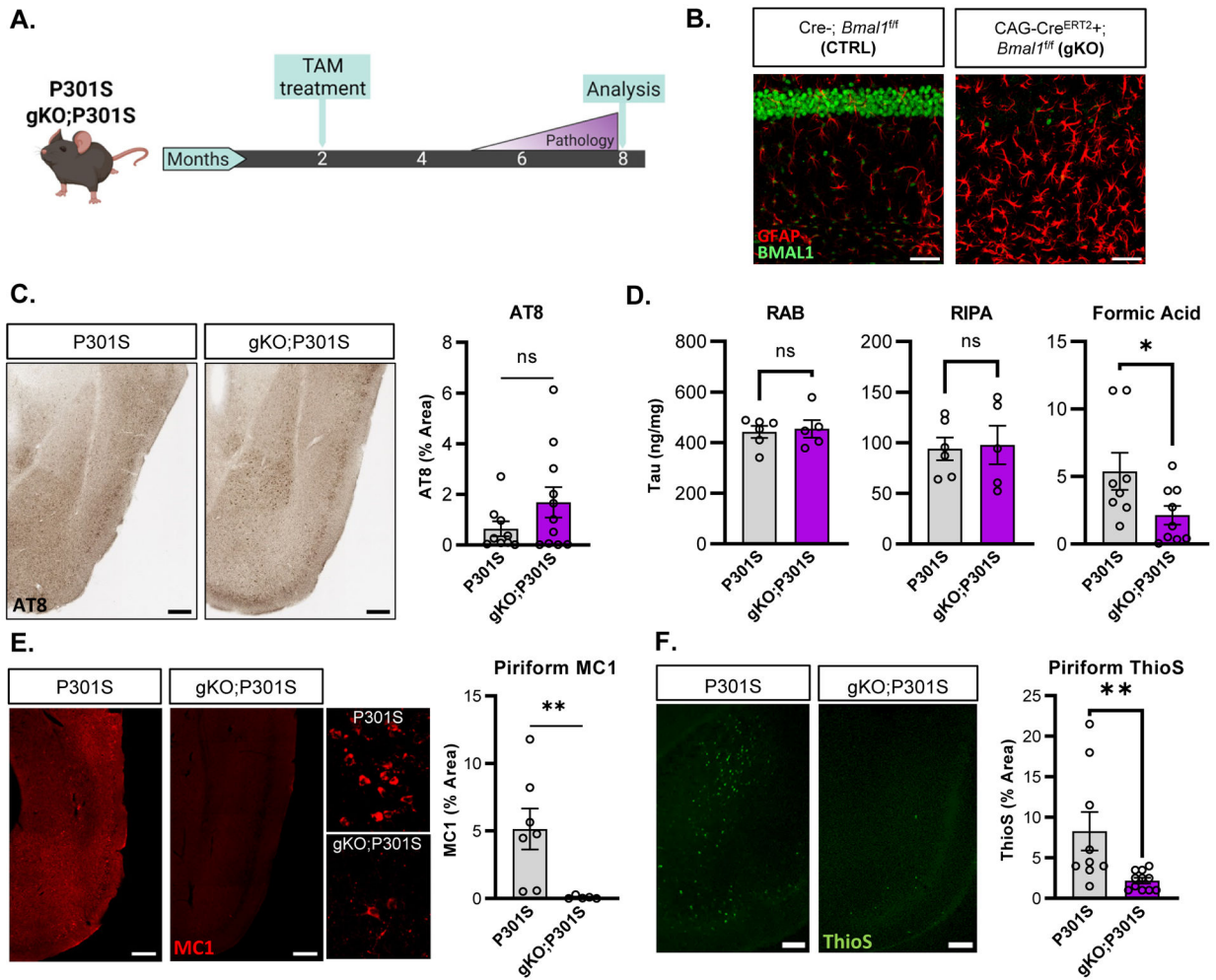


Figure 1: Global *Bmal1* deletion mitigates tau pathology.

(A) Representative images of hippocampal CA1 from CTRL (Cre-) and gKO (CAG-Cre^{ERT2+}) mice stained for GFAP (red) and BMAL1 (green). (B) Schematic of the experimental paradigm used for global *Bmal1* deletion in P301S mice. (C) Representative images and quantification of AT8 staining in piriform cortex region of P301S and gKO;P301S mice. N = 8–11 mice per group. (D) Quantification of fractionated tau between RAB (soluble tau), RIPA (slightly insoluble tau) and 70% formic acid (insoluble/aggregated tau) cortical fractions. N = 6–9 mice per group. (E) Representative images of MC1 immunoreactivity with quantification in the piriform cortex of P301S (left) and gKO;P301S mice (right). N = 6–7 mice per group. Inset shows higher magnification view. (F) Thioflavin-S staining/quantification of piriform cortex in P301S and gKO;P301S mice. All graphs in all Figures show mean±SEM unless otherwise noted. N = 9–11 mice per group. *p<0.05 or **p<0.01 by unpaired 2-tailed T-test (C,D) or Mann-Whitney test (E, F). Scale bars= 50µm (A), 200µm (C,E,F) or 20µm (E-inset).

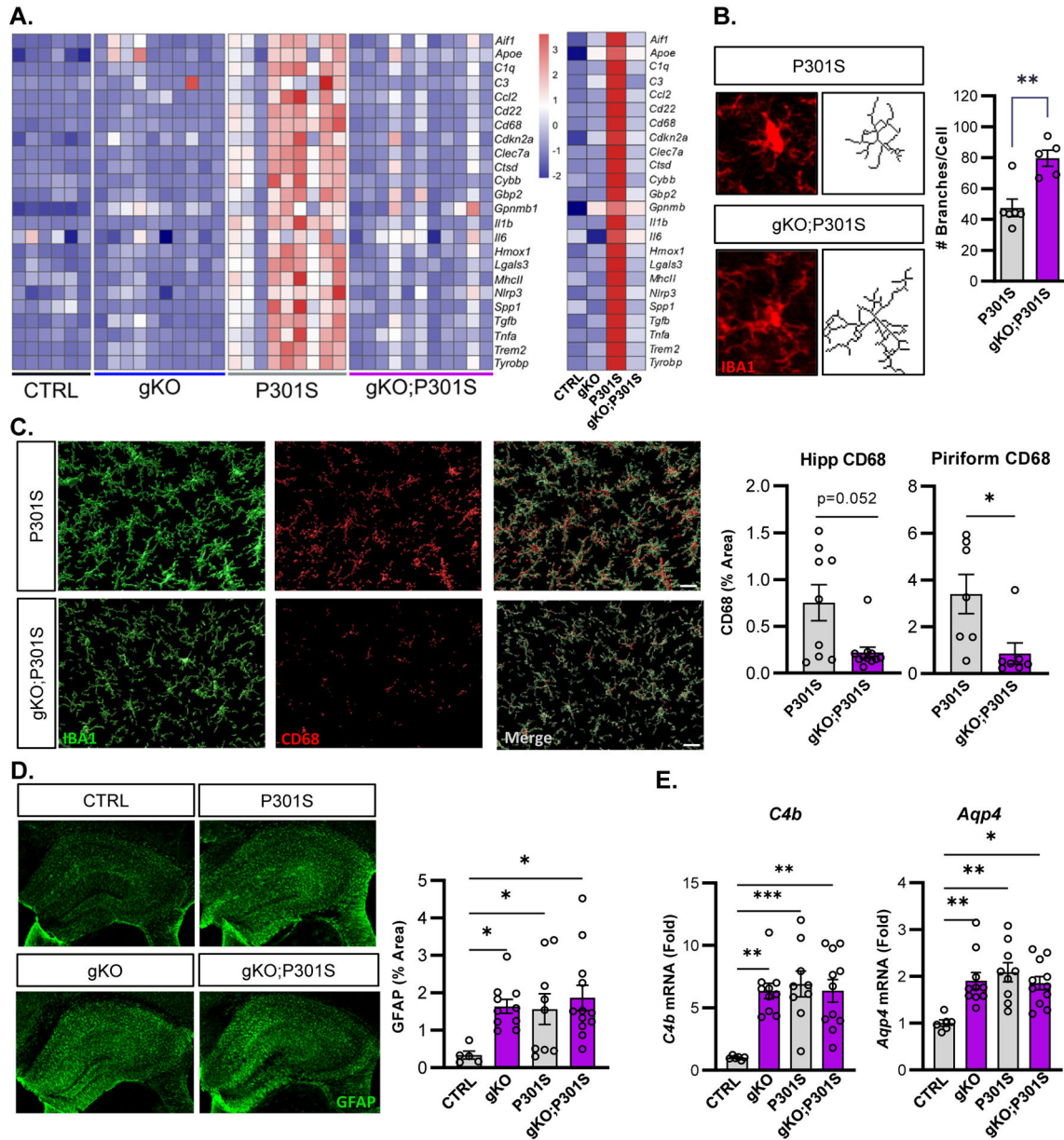


Figure 2: Global *Bmal1* deletion in P301S mice induces chronic astrogliosis and prevents microglial activation.

(A) Transcriptional analysis of inflammatory transcripts related to microglial activation in bulk cortex tissue from all four mouse genotypes. N = 6–11 mice per genotype. Averages for each genotype shown on right. (B) Representative Iba1 images and skeletonized microglia from hippocampus and quantification of branching. N = 5–6 mice per genotype with 6–9 microglia quantified per mouse. (C) Representative confocal images and quantification of CD68 immunoreactivity in the hippocampus and piriform cortex of P301S (top) and gKO;P301S mice (bottom). N = 9–11 mice per group. (D) Representative images of hippocampal GFAP immunoreactivity and quantification. (E) qPCR analysis of astrogliosis-related transcripts *C4b* and *Aqp4* across genotypes. N=5–12 mice per group. *p<0.05,

** $p < 0.01$, *** $p < 0.005$ by 2-tailed T-test (B), Mann-Whitney U test (C) or one-way ANOVA (D,E). Scale bars = 10 μm (B), 20 μm (C), or 500 μm (D).

Author Manuscript

Author Manuscript

Author Manuscript

Author Manuscript

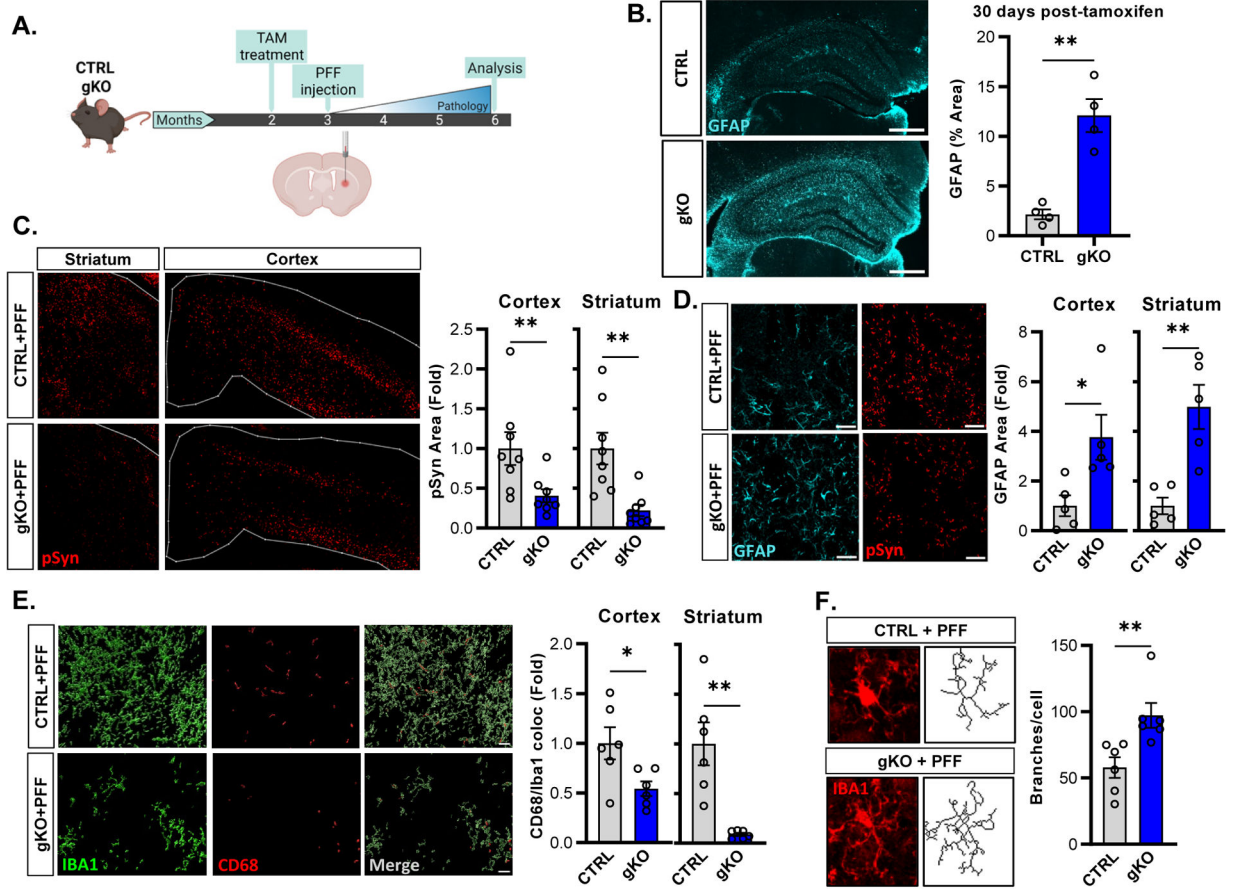


Figure 3: Global *Bmal1* deletion suppresses α -synuclein pathology and prevents microglia activation.

(A) Schematic of the experimental paradigm showing intra-striatal injection of α -Syn PFFs one month post-tamoxifen administration. (B) Representative images and quantification of astrogliosis one month after tamoxifen administration in CTRL (top) and gKO (bottom) mice. N=4 mice per group. (C) Representative images and quantification of phosphorylated α Syn (pSyn) pathology in CTRL and gKO mice at 6mo., N = 8 mice per group. (D) Representative images and quantification of pSyn (red) and GFAP (cyan) immunoreactivity in mice from C. N = 5 mice per group. (E) 3D reconstruction of confocal images of IBA1 (green) and CD68 (red) staining, with quantification of Iba1/CD68 colocalization, in mice from C. N = 6 mice per group. (F) Representative microglial Iba1 images and branching analysis with quantification in cortex from mice from C. N = 6 mice per group, n = 4–7 microglia per mouse. * $p < 0.05$, ** $p < 0.01$ by 2-tailed T-test (B,D,E-ctx,F) or Mann-Whitney U test (C,E-str). Scale bars = 500 μ m (B), 200 μ m (C-str) or 500 μ m (C-ctx), 50 μ m (D), 20 μ m (E), or 10 μ m (F).

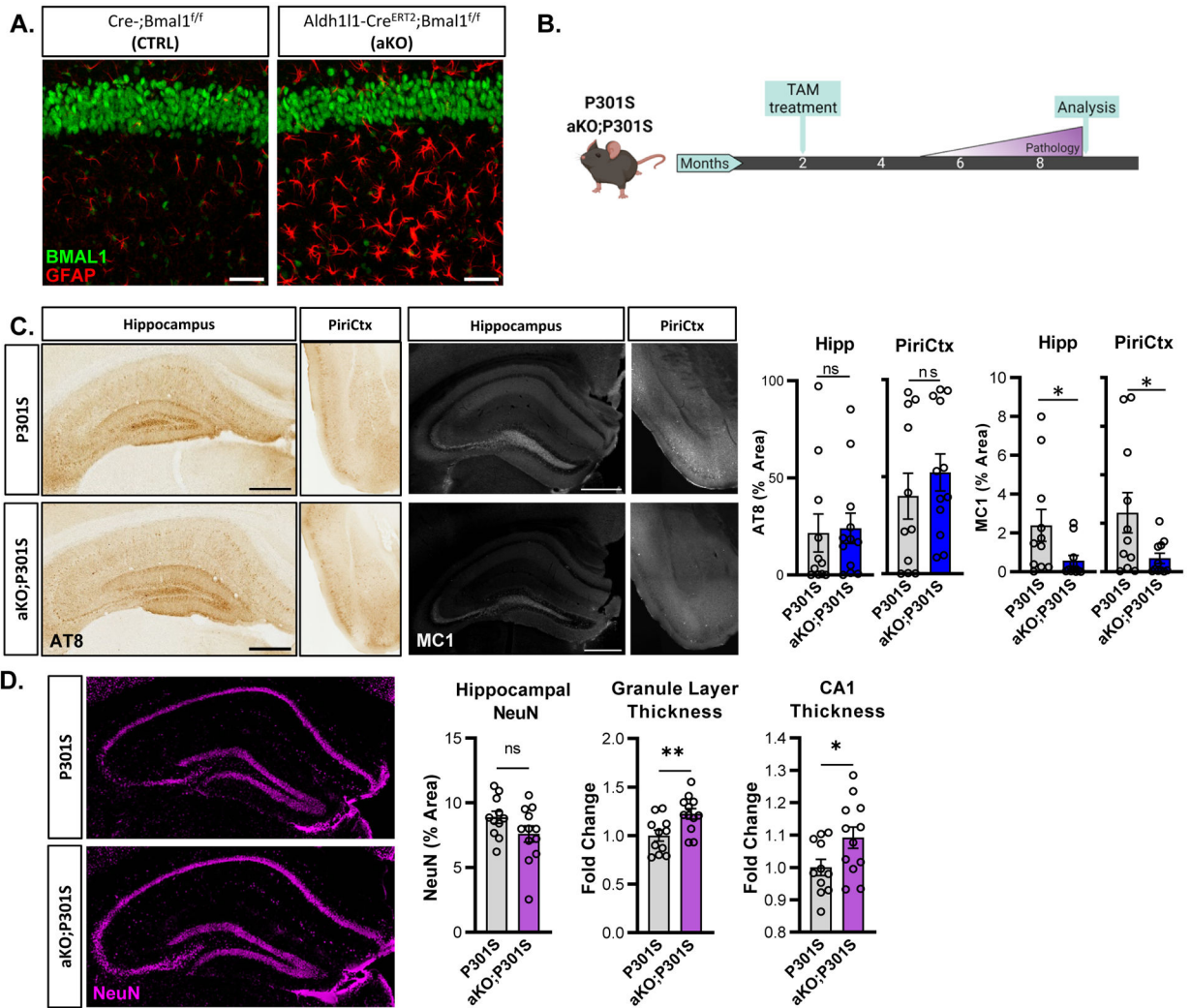


Figure 4: Astrocyte-specific *Bmal1* deletion is sufficient to induce astrogliosis and prevent tau pathology in P301S mice.

(A) Representative images of GFAP (red) and BMAL1 (green) from WT and aKO mice, CA1 region, 4 months after tamoxifen. (B) Experimental paradigm used in the tauopathy model with P301S and aKO;P301S mice. (C) Representative images and quantification of AT8 and MC1 in P301S and aKO;P301S mouse hippocampus and piriform cortex. N = 11–12 mice per group, 9 months old. (D) Hippocampal NeuN staining in P301S and aKO;P301S mice from C. with quantification of total % area and thickness of dentate gyrus granule and CA1 neuronal cell layers. *p<0.05, **p<0.01, by 2-tailed T-test (C-AT8, D) or Mann-Whitney U test (C-MC1). Scale bars = 500µm.

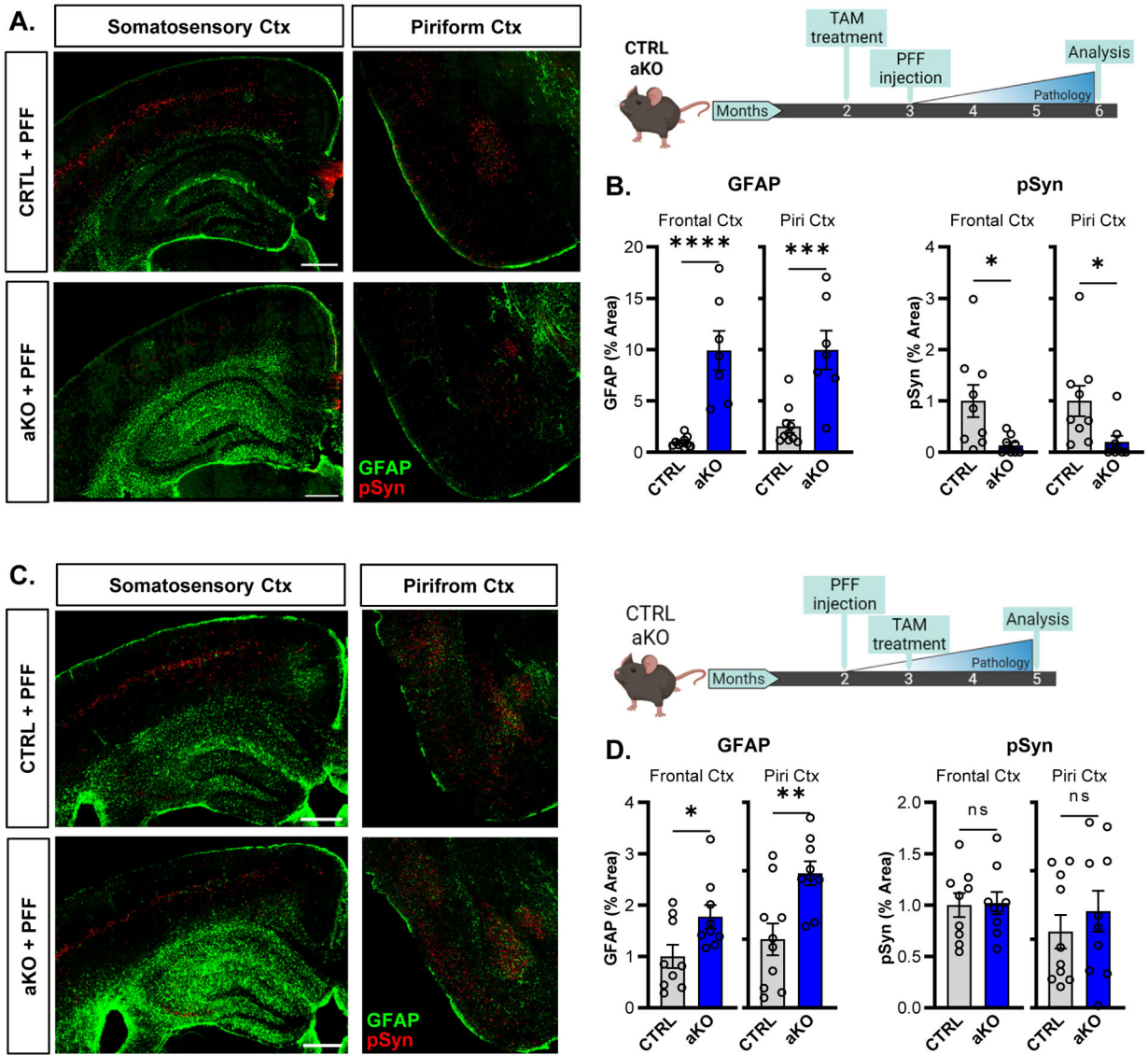


Figure 5: Astrocyte-specific *Bmal1* deletion prior to, but not after, α -synuclein PFF injection is sufficient to prevent spreading.

(A,B) Representative images (A) and quantification (B) of pSyn pathology (red) and astrogliosis (GFAP, green) in WT and aKO mice in the frontal cortex and piriform cortex at 6mo. Mice were treated with tamoxifen 1 month prior to PFF injection, as shown in experimental diagram to the right. (C,D) Representative images (A) and quantification (B) of pSyn pathology (red) and astrogliosis (GFAP, green) in WT and aKO mice in the frontal cortex and piriform cortex at 6mo. Mice were treated with tamoxifen 1 month after PFF injection, as shown in experimental diagram to the right. N= 7–9 mice per group for all experiments. *p<0.05, **p<0.01, ***p<0.001, ****p<0.0005 by Mann-Whitney U test (B) or 2-tailed T-test (D). Scale bars = 500µm.

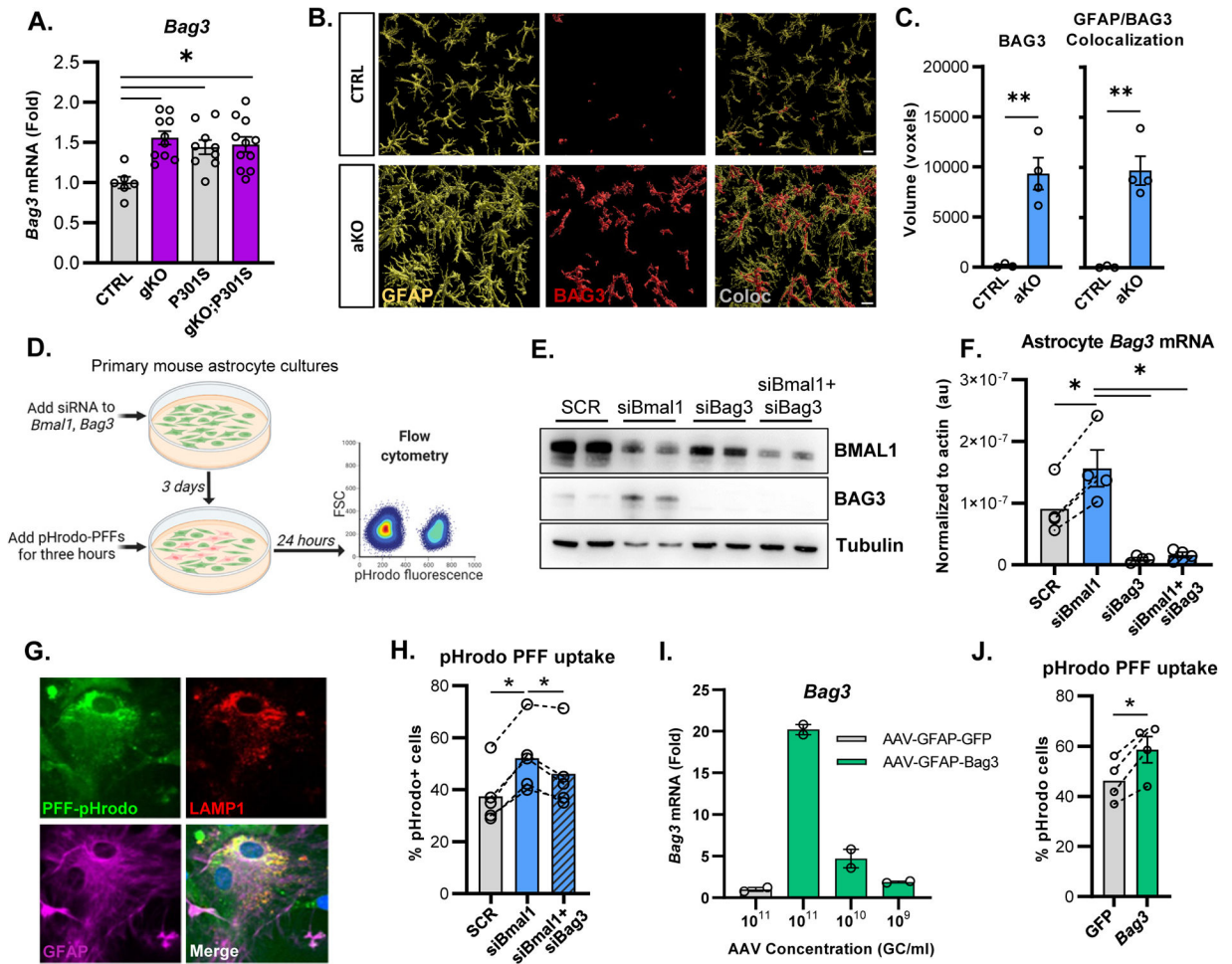


Figure 6: Astrocytic BAG3 modulates α -synuclein uptake downstream of *Bmal1*.

(A) qPCR analysis of *Bag3* in cortex of mice from Figure 2. (B) Representative confocal images of GFAP and BAG3 immunofluorescence in aKO mice. Scale bar = 10 μ m (C) Quantification of BAG3 immunofluorescence and co-localization of GFAP with BAG3 in aKO mice, using Imaris reconstruction. N = 3–4 mice per group. (D) Schematic representation of the experimental paradigm used for analyzing uptake of pHrodo-labeled α Syn PFFs. (E) Representative Western blot showing BMAL1 and BAG3 protein after siRNA treatment in astrocyte cultures. (F) qPCR analysis of *Bmal1* and *Bag3* mRNA after siRNA knockdown in primary astrocytes. (G) Representative images of primary astrocytes with phrodo-labeled PFFs and co-stained with LAMP1 and GFAP. Scale bar = 10 μ m (H) Flow cytometry analysis of the percent of phrodo-labeled PFF+ astrocytes after a 24 hour incubation. N = 5 independent experiments (I) qPCR analysis of AAV-mediated *Bag3* overexpression in primary astrocytes using a serial dilution of virus concentrations. N = 2 independent experiments. (J) pHrodo-PFF uptake in primary astrocyte culture after AAV-mediated *Bag3* overexpression. N=4 independent experiments. For F, H, and J, each circle represents the average from one independent experiment, with dotted lines connecting datapoints from that experiment. *p<0.05, **p<0.01, ***p<0.005 by 2-tailed T-test (C,J), one-way ANOVA (A,H), or repeated measures one-way ANOVA (F, H, J).

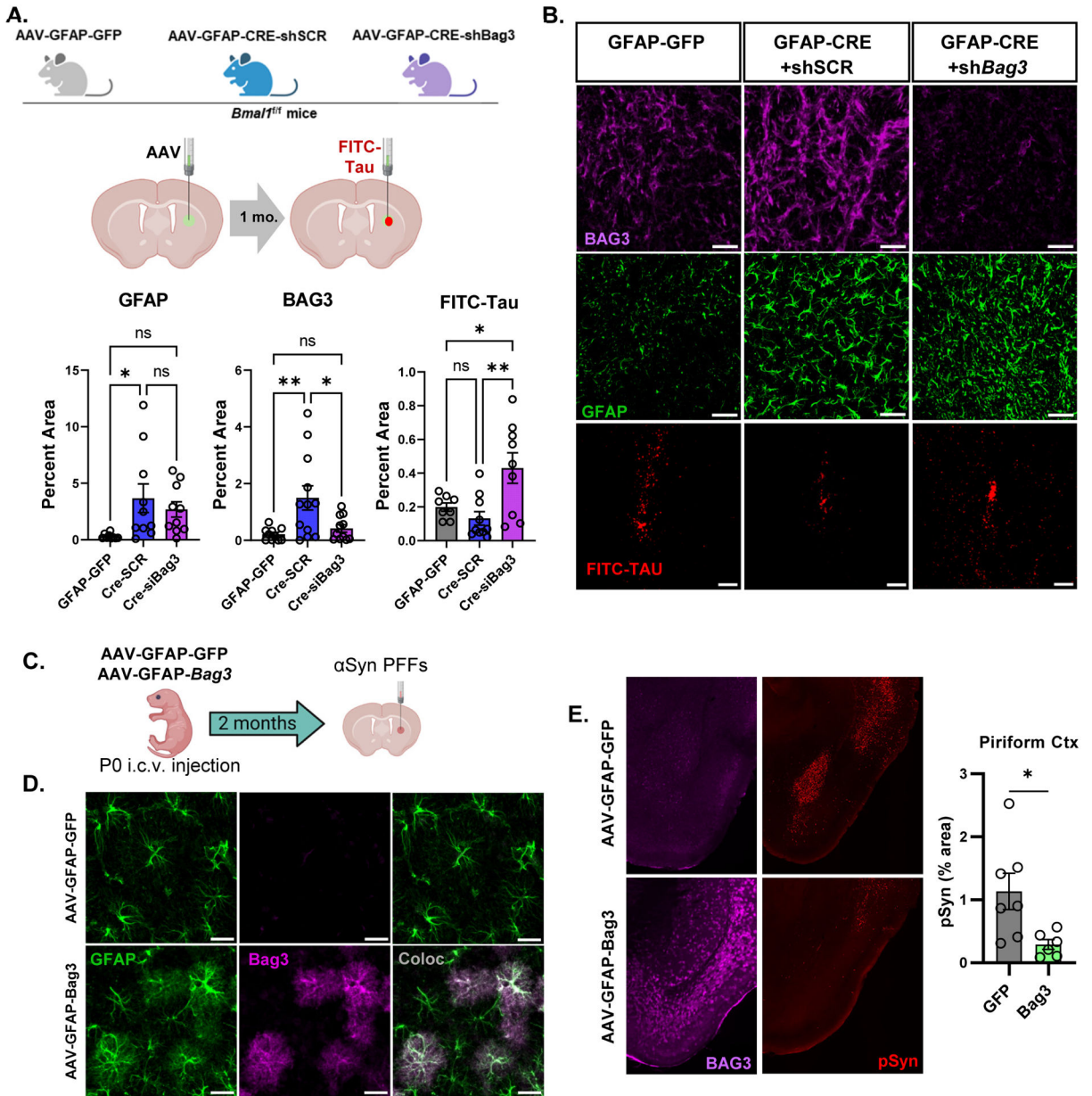


Figure 7: Astrocytic BAG3 reduces tau and αSyn pathology in vivo.

(A) Diagram depicting sequential striatal injection of viral vectors into 2 month old mice, followed by FITC-tau fibril injection 1 month later. (B) Representative images and quantification of BAG3, GFAP, and FITC-tau immunofluorescence in ipsilateral striatum 6 days after FITC-tau injection. P values in B are from one-way ANOVA with Tukey's multiple comparisons test, and are listed if <0.1. Main effect was significant with p=0.014 (BAG3) and p=0.006 (Tau). Scale bar = 100µm (C) Diagram depicting P0 i.c.v. injection of control (AAV-GFAP-GFP) or astrocyte *Bag3* overexpression vectors, followed by striatal αSyn PFF injection at 2mo, and harvest at 5 mo. (D) Images and quantification of BAG3 expression in astrocytes from (C). Scale bar = 50µm. (E) Images and quantification of BAG3

and pSyn immunofluorescence in piriform cortex of mice from (C). Scale bar = 500 μ m. In (C) and (D), $8p < 0.05$ by 2-tailed t-test.

Author Manuscript

Author Manuscript

Author Manuscript

Author Manuscript

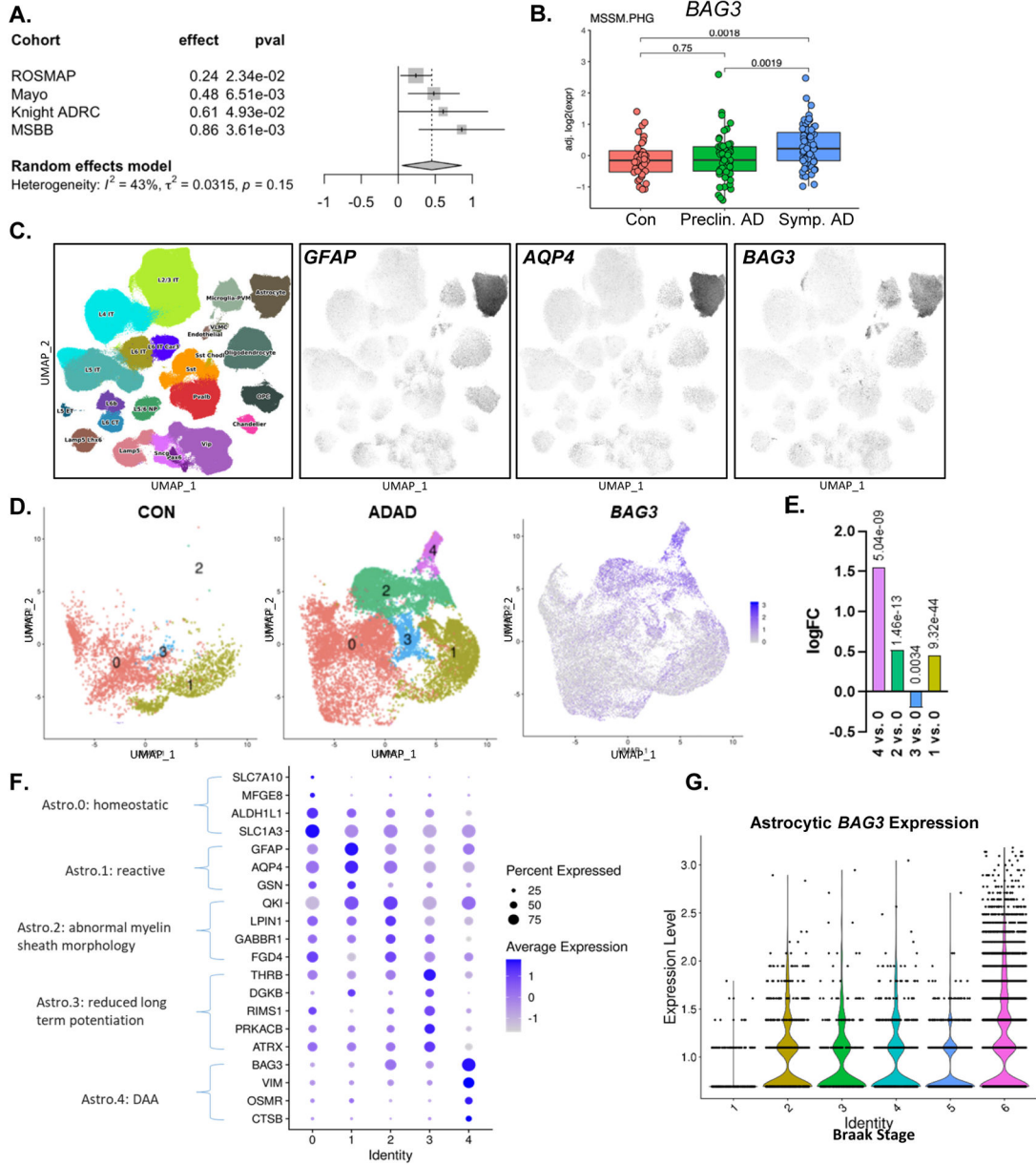


Figure 8: *BAG3* is expressed in disease-associated astrocytes in human AD.

(A) *BAG3* mRNA expression in post-mortem brain tissue from human AD patients from multiple longitudinal studies of AD. (B) *BAG3* mRNA is increase in post-mortem parahippocampal gyrus samples from patients with symptomatic AD vs. healthy controls, but not in preclinical AD. Data from Mt. Sinai Brain Bank. (C) *BAG3* is expressed primarily in human astrocytes in snRNAseq control and AD patients in the Seattle AD Brain Cell Atlas. *GFAP* and *AQP4* are shown to define the astrocyte cluster. (D) UMAP plots showing the astrocyte subclusters from control and autosomal dominant AD (ADAD) patients from the Knight ADRC. *BAG3* expression is shown on the right. (E) Dot plot showing expression levels of transcripts which define each astrocyte subcluster from (D). The subcluster number (Identity) is on the x-axis. (F) Differential expression of *BAG3*

between astrocyte subclusters from (D). The log fold change is shown on the y-axis, with each subcluster compared to Astro.0 (homeostatic) cluster. Benjamani-Hochberg-corrected p values are shown above each bar. G. Violin plot showing *BAG3* expression in astrocytes based on Braak stage (1= no pathology, 6= severe tau pathology).

Author Manuscript

Author Manuscript

Author Manuscript

Author Manuscript

KEY RESOURCES TABLE

REAGENT or RESOURCE	SOURCE	IDENTIFIER
Antibodies		
Phospho- α -synuclein (serine 129)- biotinylated (mouse)	Biologend	Cat # 825704; RRID:AB_2650683
Iba1 (goat)	Abcam	Cat # Ab5076; RRID:AB_2224402
Bmal1 (rabbit)	Novus	Cat # NB100-2288; RRID:AB_10000794
MC1 (aggregated tau) (mouse)	Dr. Peter Davies Jicha et al, 1997 ¹⁶	RRID:AB_2314773; RRID:AB_2314773
AT8 (phospho-tau)- biotinylated (mouse)	ThermoFisher	Cat # MN1020; RRID:AB_223647
CD68 (rat)	BioRad	Cat # MCA1957; RRID:AB_322219
GFAP (rabbit)	Dako/Agilent	Cat # Z0334; RRID:AB_10013382
BAG3 (rabbit)	Proteintech	Cat # 10599-1-AP; RRID:AB_2062602
HT7 (total tau)- biotinylated (mouse)	ThermoFisher	Cat # MN1000B; RRID:AB_223453
Tau5 (total tau) (mouse)	ThermoFisher	Cat # AHB0042; RRID:AB_1087687
GFAP-AlexaFluor-647 conjugate (mouse)	Cell Signaling Tech.	Cat # 3657S; RRID:AB_10693037
Tubulin (mouse)	Abcam	Cat # ab7291; RRID:AB_2241126
Bacterial and virus strains		
AAV8-GFAP-GFP	This paper	N/A
AAV8-GFAP-Bag3	This paper	N/A
Php.eb-AAV-GFAP-Cre-shSCR	This paper	N/A
Php.eb-AAV-GFAP-Cre-shBag3	This paper	N/A
Biological samples		
Chemicals, peptides, and recombinant proteins		
pHrodo Red succinimdy ester	ThermoFisher	Cat # P36600
Human FITC-tau-441	rPeptide	Cat # T-1113-1
Thioflavine S	Sigma-Aldrich	Cat # T1892
Human recombinant alpha-synuclein	In house	N/A
3,3 diaminobenzidine tablets	Sigma	Cat # D4293
Lipofectamine RNAiMax	ThermoFisher	Cat # 13778075
Critical commercial assays		
Deposited data		
Bulk RNAseq, cortex, Aldh111-Cre+;Bmal1(f/f) vs. Cre-;Bmal1(f/f) controls	McKee et al. ⁷	GSE227063
Wang et al AD microarray data	Wang et al. ³⁰	GSE84422
Seattle Alzheimer Disease Brain Cell Atlas	Allen Brain Map	https://portal.brain-map.org/explore/seattle-alzheimers-disease
ADAD snRNAseq (Fig. 8)	Brase et al. ³¹	http://ngi.pub/SNARE/
Knight-ADRC snRNAseq (Fig. 8)	Brase et al. ³¹	http://ngi.pub/SNARE/
Knight-ADRC (Fig. 8)	Knight-ADRC – bulk RNA-seq Data	https://www.niagads.org/datasets/ng00083

REAGENT or RESOURCE	SOURCE	IDENTIFIER
Mayo (Fig. 8)	The Mayo RNAseq Study (MayoRNAseq)	https://doi.org/10.7303/syn5550404
ROSMAP (Fig. 8)	The Religious Orders Study and Memory and Aging Project (ROSMAP) Study	https://doi.org/10.7303/syn3219045
MSBB (Fig. 8)	The Mount Sinai Brain Bank (MSBB) study	https://doi.org/10.7303/syn3159438
Sn-ATAC-Seq (Supplemental Fig 8)	Single nucleus ATAC-seq data from the SEA-AD cohort in the UCSC Genome Browser for the SNP	shorturl.at/csxE2
PD GWAS data (Supp Fig. 9)	Greene et al. ³³	https://pdgenetics.shinyapps.io/GWASBrowser/
Experimental models: Cell lines		
Primary mouse astrocytes	In house	N/A
Experimental models: Organisms/strains		
<i>CAG-Cre^{ERT2}</i> mice; B6.Cg-Tg(CAG-cre/Esr1*)5Amc/J	Jackson Labs	Cat # 004682; RRID: IMSR_JAX:004682
<i>Aldh111-Cre^{ERT2}</i> mice; B6N.FVB-Tg(Aldh111-cre/ERT2)1Khakh/J	Jackson Labs	Cat # 031008; RRID: IMSR_JAX:031008
<i>CX3CR1^{ERT2}</i> mice; B6.129P2(Cg)-Cx3cr1tm1Litt/J	Jackson Labs	Cat # 005582; RRID: IMSR_JAX:005582
<i>Bmal1^{fllox/fllox}</i> mice; B6.129S4(Cg)-Bmal1tm1Weit/J	Jackson Labs	Cat # 007668; RRID: IMSR_JAX:007668
<i>hMAPT</i> P301S PS19; B6;C3-Tg(Prnp-MAPT*P301S)PS19Vle/J	Jackson Labs	Cat # 008169; RRID: IMSR_JAX:008169
Timed-pregnant CD1 mice	Charles River Labs	Cat # 022
Oligonucleotides		
Mouse <i>Bmal1</i> siRNA, Dharmacon ONTARGET+ SMARTpool	Horizon Discovery	Cat # L-040483-01-0005
Mouse non-targeting siRNA, Control 1, Dharmacon ONTARGET+ SMARTpool	Horizon Discovery	Cat # D-001810-01-05
Mouse <i>Bag3</i> siRNA, Dharmacon ONTARGET+ SMARTpool	Horizon Discovery	Cat # L-064450-00-0005
C4b Taqman primer	ThermoFisher	Mm00437893_g1
Gfap Taqman	ThermoFisher	Mm01253033_m1
Aqp4 Taqman	ThermoFisher	Mm00802131_m1
Nr1d1 Taqman primer	ThermoFisher	Mm00520708_m1
Bag3 Taqman primer	ThermoFisher	Mm00443474_m1
<i>Bmal1</i> /Arntl Taqman primer	ThermoFisher	Mm00500223_m1
Additional primers listed in Table S2		
Recombinant DNA		
<i>Bag3</i> cDNA	Mammalian Gene Collection	Enztrez ID 29810
Software and algorithms		
GraphPad Prizm v.9.3.1	GraphPad Software	RRID:SCR_002798
ImageJ	NIH	RRID:SCR_003070
Imaris	Oxford Instruments	RRID:SCR_007370
pheatmap	R package	RRID:SCR_016418

REAGENT or RESOURCE	SOURCE	IDENTIFIER
DEseq2	Love et al. ⁶¹	RRID:SCR_015687
ggplot2	Wickham, H. ⁶²	RRID:SCR_014601
Picard	Broad Institute	RRID:SCR_006525
TOPMed RNAseq pipeline	NIH	RRID:SCR_015677
Other		

Author Manuscript

Author Manuscript

Author Manuscript

Author Manuscript